Summer 2024

Investigating the Role of Bias and Sample Incompleteness in Gamma-ray Burst Studies

Christopher M. Bryant
University of Texas at Arlington

Investigating the Role of Bias and Sample Incompleteness in Gamma-ray Burst Studies

by

Christopher Michael Bryant

A dissertation presented for the degree of

Doctor of Philosophy

Department of Physics

University of Texas at Arlington

August 2024

ABSTRACT

Investigating the Role of Bias and Sample Incompleteness in Gamma-ray Burst Studies

Christopher Michael Bryant, Ph.D.

University of Texas at Arlington, 2024

Supervising Professor: Amir Shahmoradi

Gamma-ray bursts (GRBs) are the most energetic stellar explosions that have been observed in the universe. Due to their high energy and the collimated nature of the burst, they can be detected at cosmological distances. In addition to the prompt gamma-ray emission, an afterglow is usually detected at longer wavelengths, which can allow for a redshift calculation and localization of the host galaxy. Understanding GRBs is not only critical for determining the physics driving their progenitors, but for probing the high-redshift cosmos.

The space-based satellites that detect GRBs have complex triggering mechanisms, and accounting for their limitations (e.g., detection thresholds) is vital for drawing inferences from the data that they collect. Likewise, the statistical methods employed to analyze the data should be very carefully considered, so as to not unintentionally affect the conclusions drawn from the data.

In this dissertation, I present two studies that reconsider conclusions drawn from GRB datasets. The first study is a reanalysis of several recent studies that concluded there is a correlation between the luminosity/energetics of long GRBs (LGRBs) and their redshift. We demonstrate that the inferred correlations are likely significantly affected by an underestimation of the detection threshold. In the second study, the use of an apparent plateau in the duration distribution of

LGRBs as evidence for the collapsar model is reexamined. We demonstrate that multiple aspects of the statistical properties of the dataset and methodologies used provide opportunity for the generation of a plateau that has no physical origin. Collectively, these studies aim to enhance the reliability of GRB studies by identifying and addressing the roles of bias and sample incompleteness.

"Ad astra per aspera"

To the stars, through adversity

Acknowledgements

First and foremost, I would like to express my deepest gratitude to my research advisor, Dr. Amir Shahmoradi. His unwavering belief in my abilities has been a constant source of motivation throughout this journey. When I was forced to take a leave of absence during a particularly challenging period in my life, his support never wavered, and his understanding and compassion during that difficult time were invaluable. His encouragement gave me the confidence to return and complete the Ph.D. that I have dedicated so many years of hard work toward. Next, I would like to thank the members of my committee, Drs. Qiming Zhang, Manfred Cuntz, Nevin Weinberg, and Sangwook Park, as well as the head of the department, Dr. Alex Weiss, for their support during my time at UTA. Finally, I would like to thank my peers in this program who made this journey a memorable shared experience, most notably: Dr. Sarah Hernandez, Crystal Red Eagle, Ashley Shukayr, Dr. Richard Bonde, and Joshua Osborne.

Dedicated to my mom and my sister, whose memory, like the stars,

continues to light my path through the vast cosmos of life and discovery

Contents

List of Figures

List of Tables

1 Introduction

Gamma-ray Bursts (GRBs) are the most violent and energetic stellar explosions in the known universe, piercing the cosmos in a collimated beam of gamma-rays. With a typical isotropic gamma-ray luminosity of ~10^{51} – 10^{53} erg s^{-1}, these cataclysmic events can radiate as much energy as the lifetime energy output of the Sun within less than a second (Atteia et al., 2017). Because these immense energies are confined to a tight beam, GRBs can be detected at very high redshift (the current record being $z = 9.4$ with a lookback time of ~13.2 Gyr for GRB090429B) (Cucchiara et al., 2011). They are followed by an afterglow emission at longer wavelengths that allow for multi-spectral analysis (Kouveliotou et al., 1993).

1.1 History

The discovery of GRBs dates back to the Cold War era in the early 1960s. Amid escalating nuclear tests by the United States and the Soviet Union, both nations recognized the unsustainable nature of such activities. This led to the signing of the Limited Nuclear Test Ban Treaty in 1963, which prohibited nuclear tests in the atmosphere, outer space, and underwater. Despite the treaty, mistrust between the U.S. and the Soviet Union persisted, particularly concerning potential nuclear tests in outer space. In response, the U.S. Department of Defense initiated the Vela satellite program. These military satellites, launched in pairs starting

in 1963, were designed to detect nuclear test signatures in space and triangulate their origins (London III, 1993).

In 1967, the Vela satellites detected a gamma-ray signature in space that was determined to have not originated from nuclear tests. The data, declassified in 1973, revealed that it, and 15 similar detections, were of extra-solar origin. The signals were brief (<0.1 – 30 s) and isotropically distributed on the celestial sphere (Klebesadel, Strong, and Olson, 1973; Strong, Klebesadel, and Olson, 1974).

Following this discovery, there would be minimal observational advancements until 1991, when NASA launched the Compton Gamma-ray Observatory (*Compton*), whose main objectives included not only detecting many more GRBs but, crucially, localizing them more clearly. The instrument responsible for this on-board *Compton* was the Burst and Transient Source Experiment (BATSE). Up to that point, fewer than a hundred GRBs had been detected; *Compton* would go on to detect well over 2000 during its operational lifetime (Fishman et al., 1994; Gehrels, Chipman, and Kniffen, 1993). Eventually, other satellites would be launched that were also capable of observing GRBs, among them the Neil Gehrels Swift Observatory (*Swift*) in 2004 and the Fermi Gamma-ray Space Telescope (*Fermi*) in 2008.

1.2 Observational Properties

GRBs are detected across the entire electromagnetic spectrum through a combination of space-based and ground-based telescopes. This section outlines the features, and utility, of both the prompt emission and afterglow of GRBs, providing context for the current thesis.

1.2.1 Prompt Emission

The prompt emission phase of a GRB is characterized by a sudden and intense burst of photons in the hard-X-ray/soft-gamma-ray band, typically lasting from milliseconds to several minutes. This phase is primarily observed using space-based telescopes, as Earth's atmosphere is opaque to gamma-rays. Two key aspects of the prompt emission are the light curve and the spectral properties:

Light Curves

The light curves of GRB prompt emissions are notably irregular and complex, with no two being identical; see Figure 1.1 for an example set from BATSE. There is significant variation in almost every property: the number of pulses can vary from one to multiple, and they can be symmetric or demonstrate a "fast rise exponential decay" (FRED) behavior; the variability can be smooth or display extreme millisecond-scale changes; the duration can vary from mere milliseconds to thousands of seconds (Pe'Er, 2015). Some GRBs even have weak precursor events to the main burst (Koshut et al., 1995).

The total duration of the GRB prompt emission is commonly defined by the parameter T_{90}, which is the interval during which 5% and 95% of the total fluence is registered by the detector. It was discovered with the BATSE dataset in the 1990s that the T_{90} distribution is bimodal for a large number of GRBs, suggesting two separate populations: short GRBs (SGRB) and long GRBs (LGRB); see Figure 1.2. Working off of the first year of observational data from BATSE, Kouveliotou et al. (1993) suggested the delimitation of these two populations occur at $T_{90} = 2$ s, which results in ~1/4 of the BATSE catalog being classified as SGRBs and ~3/4 as LGRBs. When the *Swift* and *Fermi* catalogs are included (as of July 2024), these ratios shift slightly to ~1/5 and ~4/5, respectively. Ultimately, LGRBs are observed several times more often than SGRBs. When these three catalogs are

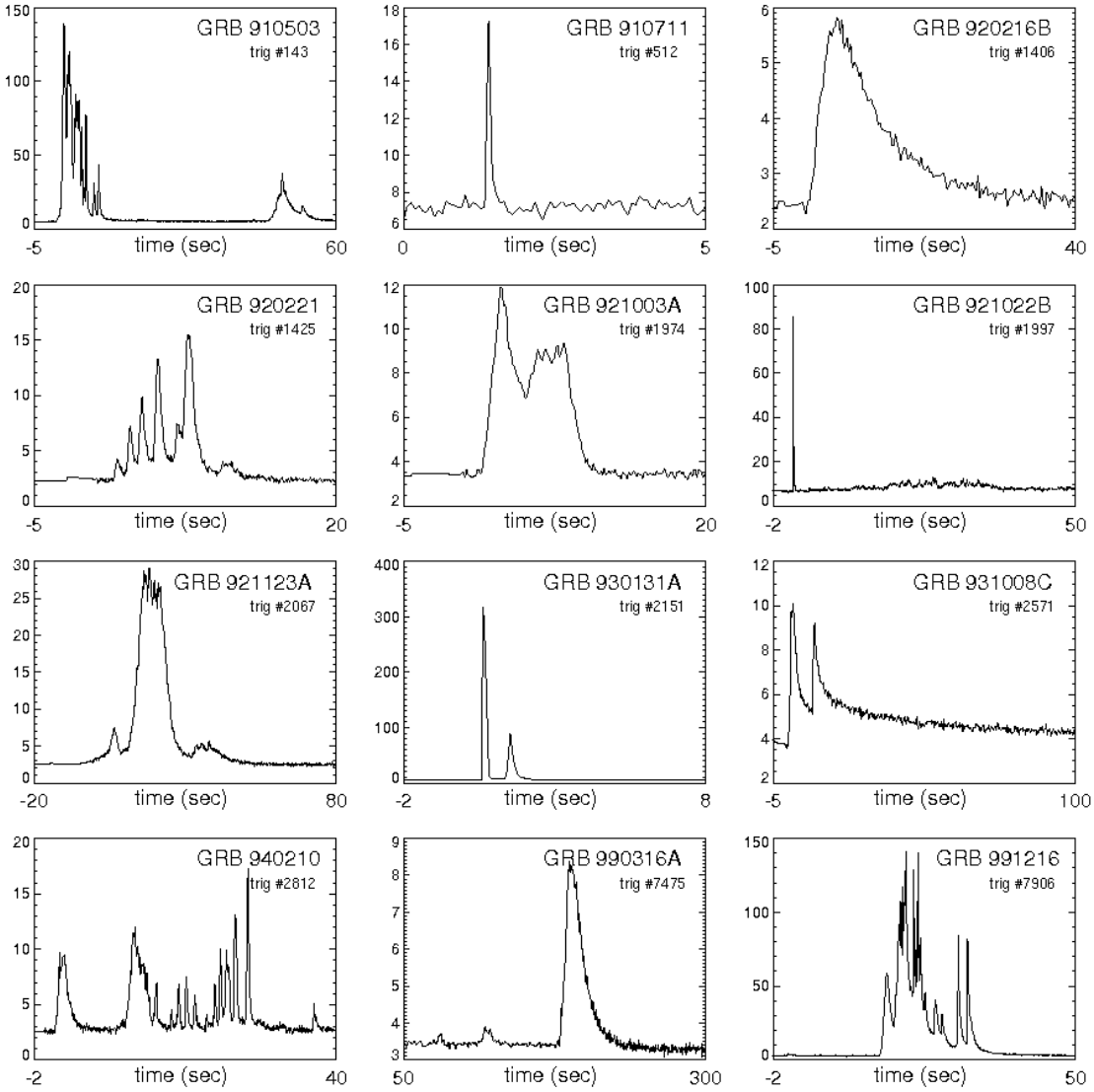

Figure 1.1: The variability of light curves as seen in this selection of 12 GRBs detected by BATSE. Note the significant variations in duration, number of peaks, and smoothness. Figure credit: Daniel Perley with data from the public BATSE archive.

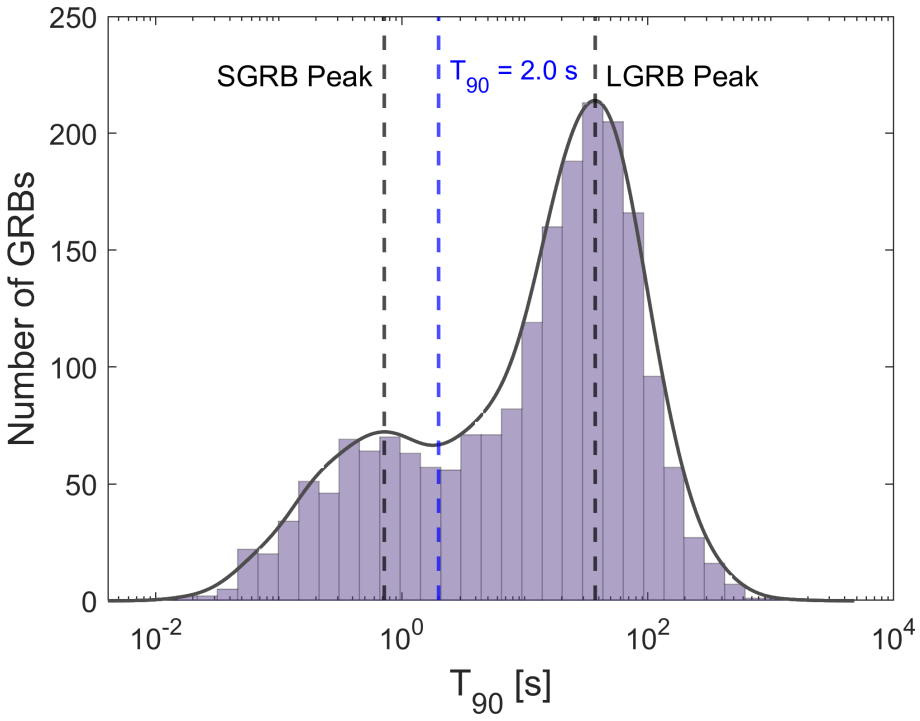

Figure 1.2: The bimodal distribution of durations as seen in the BATSE dataset of 2041 GRBs. Events below the threshold of $T_{90} = 2$ s (dashed blue line) are classified as SGRBs, and those above as LGRBs.

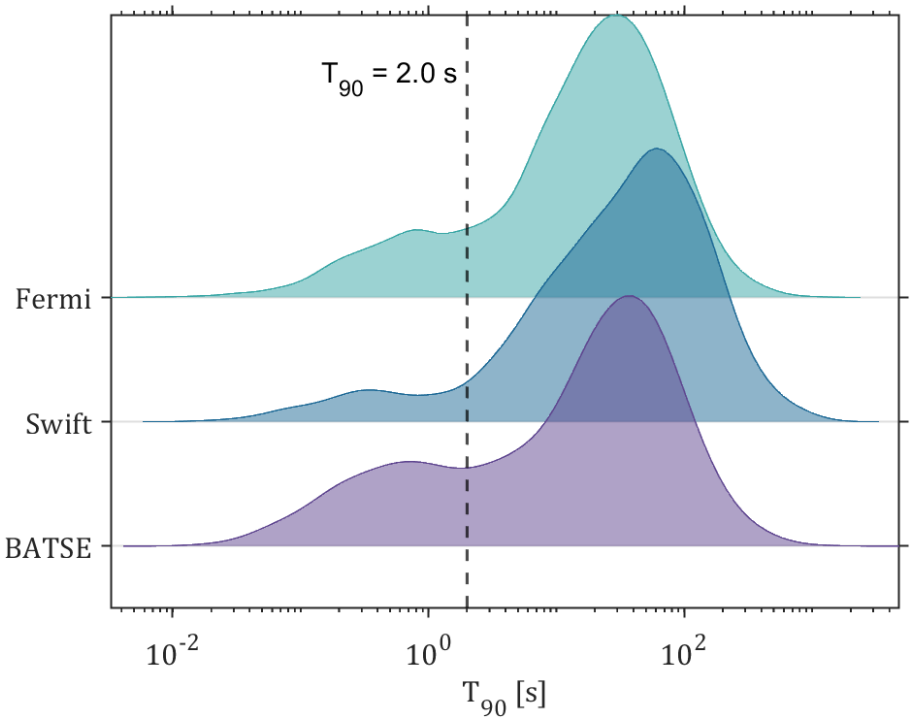

Figure 1.3: A comparison of the shape of the T_{90} duration distributions of the BATSE, *Swift*, and *Fermi* catalogs (as of July 2024). Shapes extracted via kernel density estimate.

visualized against one another (Figure 1.3), it is noticeable that the $T_{90} = 2\,\mathrm{s}$ delimitation does not as accurately divide the populations of the *Swift* and *Fermi* datasets as it does BATSE's.

Spectral Properties

Typically, the prompt emission is observed to be an X-ray/gamma-ray non-thermal spectrum, whose spectral shape can be well-described by the empirical Band function. Defined by Band et al. (1993) as a smoothly connected combination of two power laws, it is characterized by a low-energy segment and a high-energy segment, with a peak energy where the transition occurs. It is defined as follows:

$$N(E) = \begin{cases} A \left(\frac{E}{100\,\mathrm{keV}}\right)^{\alpha} \exp\left(-\frac{E}{E_0}\right), & \text{if } E < (\alpha-\beta)E_0 \\ A \left[\frac{(\alpha-\beta)E_0}{100\,\mathrm{keV}}\right]^{(\alpha-\beta)} \exp(\beta-\alpha) \left(\frac{E}{100\,\mathrm{keV}}\right)^{\beta}, & \text{if } E \geq (\alpha-\beta)E_0 \end{cases} \tag{1.1}$$

where

$$E_p = (2+\alpha)E_0$$

In this equation, $N(E)\mathrm{d}E$ is the number of photons in the energy bin $\mathrm{d}E$, and A is the normalization constant [photons s^{-1} cm^{-2} keV^{-1}]. α is the low-energy photon index, and describes the spectral slope at energies lower than the peak energy. It typically ranges between -1 and -2. β is the high-energy photon index, and defines the spectral slope at energies higher than the peak energy. Values for it typically fall between -2.5 and -3.5. E_0 is the break energy [keV] that determines where the spectral transition occurs, and E_p is the peak energy [keV] of the νF_ν spectrum. E_p varies significantly among GRBs, and typically falls in the range of 100 keV to a few MeV.

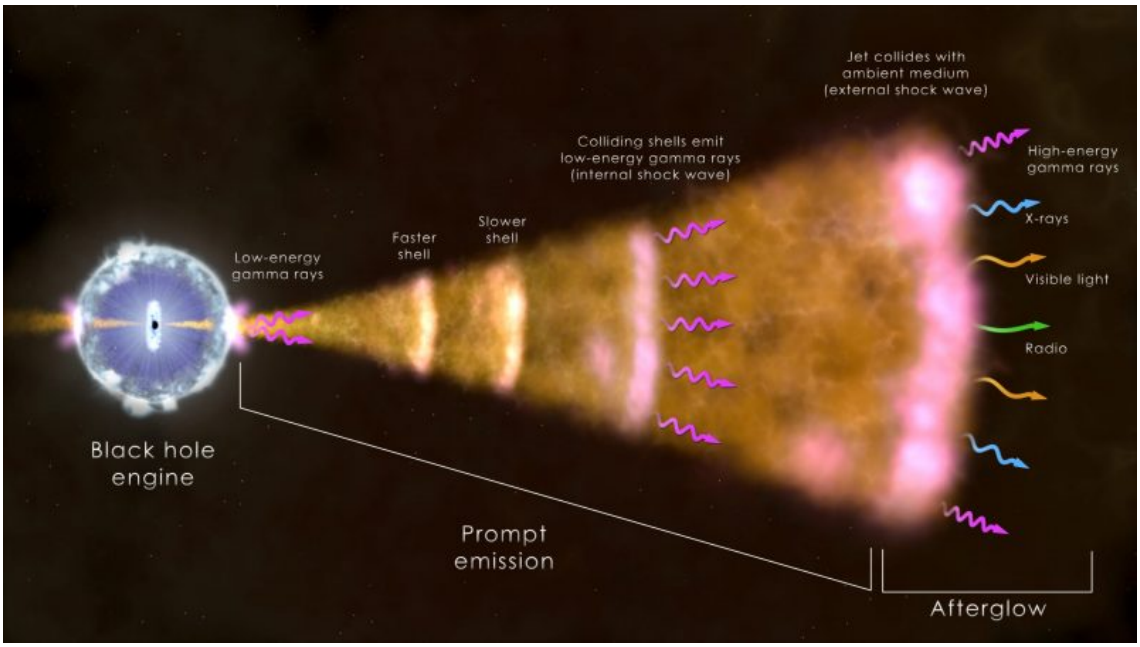

Figure 1.4: The fireball model for LGRBs. Figure credit: NASA's Goddard Space Flight Center

1.2.2 Afterglow

After the intense prompt emission phase of a GRB, a longer-lasting afterglow is typically observed across the remainder of the EM spectrum. Unlike the prompt emission that can last up to several minutes, the afterglow can last for weeks, months, or in rare cases, years. The afterglow emission is attributed to the interaction between the jetted relativistic outflow and the surrounding interstellar medium (Mészáros and Rees, 1997); see Figure 1.4. This interaction creates an external shock, which is responsible for the observed afterglow. The presence of highly beamed jetted outflows has been empirically confirmed through the identification of the jet break feature within the afterglow light curves.

GRBs typically exhibit jet opening angles of only a few degrees (Panaitescu and Mészáros, 1999; Rhoads, 1997). As we are observing the GRB at a particular viewing angle, the beaming cone of the relativistic jet eventually widens enough that we can start seeing the edges of the jet. At this point, the afterglow light

curve exhibits a characteristic steepening, known as a jet break (Rhoads, 1999). This phenomenon is primarily geometric in nature and, as such, does not alter the emission spectrum; it manifests across all observed wavebands, from X-ray to radio.

Optical and infrared afterglows are crucial for localizing GRBs and identifying their host galaxies. The brightness and duration of the optical afterglow can vary significantly, influenced by factors such as the angle of the jet relative to the detector, the density of the surrounding medium, and the presence of dust extinction. These observations are essential for determining the redshift of GRBs, thereby providing information about their distance.

1.3 Models

Current theoretical models suggest that SGRBs are generated by kilonovae[1], which result from the merger of compact binary systems, such as neutron star-neutron star (NS-NS) or neutron star-black hole (NS-BH) pairs (Eichler et al., 1989; Nakar, 2007). During these cataclysmic events, the violent coalescence of the compact objects leads to the ejection of matter and the formation of a highly relativistic jet. This jet, if aligned with our line of sight, emits intense gamma rays that can be detected by gamma-ray observatories. The alignment and subsequent detection are contingent on the orientation of the jet relative to Earth, which is critical for the observability of the SGRB.

The first confirmation of this model came in 2017, with the simultaneous detection of gravitational waves (GW) and radiation across the electromagnetic spectrum. The event began with the detection of gravitational wave signal GW170817 by the LIGO/Virgo collaboration, lasting approximately 100 seconds. ~1.7 sec-

[1] A kilonova is named as such because it reaches a peak brightness of about 1000 times that of a nova while being 10-100 times less luminous than a supernova (Metzger et al., 2010).

onds after the merger time, the short duration GRB 170817A was detected by *Fermi* and the *International Gamma-Ray Astrophysics Laboratory* (INTEGRAL). With all eyes on the sky, an intense observing campaign followed to locate the expected optical emission. Less than 11 hours later, astronomical transient AT 2017gfo was found in the galaxy NGC 4993 at ~40 Mpc. In the coming days and weeks, dozens of ground-based and space-based detectors captured the afterglow emissions. The event confirmed that at least some SGRBs are produced by kilonovae, heralding in the age of multi-messenger astronomy (Abbott et al., 2017b; Goldstein et al., 2017; Savchenko et al., 2017a).

LGRBs are believed to be caused by the death of massive stars[2], specifically, those that end in core-collapse supernovae (Woosley and Bloom, 2006; Woosley, 1993). The larger a star is, the higher its core pressure and the higher the species of elements it can fuse up to. However, once the core begins producing iron, the reaction can go no further, as the reactions consume energy instead of producing it. Unable to withstand the pressure of the stellar envelope, the core rapidly collapses into a black hole, as the rest of the star is blasted apart in a spectacular supernova explosion (Glendenning, 2012). The black hole launches polar jets that then must drill through the expanding shell of ejecta (MacFadyen and Woosley, 1999; MacFadyen, Woosley, and Heger, 2001), sending a tightly collimated beam of radiation into space. Some theories propose this is also possible for a newly-formed magnetar (Usov, 1992; Zhang and Mészáros, 2001).

This collapsar model has garnered substantial observational support through the confirmed association of approximately half a dozen LGRBs with broad-line Ic supernovae, which have been spectroscopically verified. Additionally, photometric evidence of underlying supernovae has been observed in approximately two dozen more cases, further bolstering the connection between LGRBs and su-

[2]generally having mass $M \geq 30 M_{\odot}$

pernovae (Galama et al., 1998; Hjorth et al., 2011; Hjorth et al., 2003; Stanek et al., 2003; Woosley and Heger, 2006). Beyond these direct associations, there is significant indirect evidence linking LGRBs to massive stars. This evidence is derived from the identification of LGRB host galaxies as environments characterized by intense star formation. Moreover, LGRBs are often localized within the most active star-forming regions of these galaxies, strongly suggesting that LGRBs are the end products of the deaths of supermassive stars.

1.4 Organization of Thesis

The primary focus of this thesis is to improve the reliability of GRB studies by identifying and addressing the influence of bias and sample incompleteness. This research endeavors to achieve a more precise understanding of GRBs and to refine the methodologies employed in their analysis. The thesis is structured as follows: Chapter 2 reproduces my paper on how underestimating the detector threshold can affect the perceived correlations between redshifts and the luminosity of LGRBs. Chapter 3 presents a reproduction of my paper examining how observed plateaus in GRB duration datasets, often attributed to the physics of the progenitor, may instead arise from purely statistical factors. Finally, Chapter 4 provides a summary and concluding remarks.

2 HOW UNBIASED STATISTICAL METHODS LEAD TO BIASED SCIENTIFIC DISCOVERIES: A CASE STUDY OF THE EFRON-PETROSIAN STATISTIC APPLIED TO THE LUMINOSITY-REDSHIFT EVOLUTION OF GAMMA-RAY BURSTS

Authors: Bryant, Christopher Michael, Joshua Alexander Osborne, and Amir Shahmoradi

Published: Monthly Notices of the Royal Astronomical Society 504.3 (2021): 4192-4203.

2.1 Introduction

Gamma-Ray Bursts (GRBs) are the most violent and energetic stellar explosions in the known universe. They radiate huge amounts of gamma-ray energy, comparable to the lifetime energy output of the sun, over a short period of time and are often followed by an afterglow at longer wavelengths (e.g., Gehrels, Ramirez-Ruiz, and Fox, 2009; Mészáros, 2006; Zhang, 2007). With their energy concentrated in a collimated beam, they can be seen at much higher redshifts than supernovae (SNe). Amongst other things, GRBs are excellent tools to probe the Star Formation Rate (SFR) of the early as well as the recent universe.

GRBs are generally divided into two categories: Long-soft GRBs (LGRBs) with $T_{90} \gtrsim 2\ [s]$, and Short-hard GRBs (SGRBs) with $T_{90} \lesssim 2\ [s]$.[1] These values are based on population statistics of the *Compton Gamma Ray Observatory*'s Burst and Transient Source Experiment (BATSE) detector, which was decommissioned in 2000 (Kouveliotou et al., 1993; Shahmoradi, 2013a,b; Shahmoradi and Nemiroff, 2011b, 2015). LGRBs are believed to be the result of the collapse of massive stars into a black hole (Woosley, 1993), while SGRBs are theorized to be the result of the merger of two neutron stars or of a neutron star and a black hole (Eichler et al., 1989).

Current research attempts to infer an accurate description and distribution profile of various GRB characteristics, in particular, the class of LGRBs due to their abundant redshift measurements compared to the SGRB class. A recent focus in the community has been on the potential cosmological evolution of LGRB luminosity/energetics L_{iso}/E_{iso} with redshift, as well as estimating the cosmic rates of LGRBs. A popular technique to constrain these is based on the non-parametric method of Efron-Petrosian (Efron and Petrosian, 1992; Petrosian, 2002), which is

[1] T_{90} is the duration over which a burst emits from 5 - 95% of its total measured gamma-ray photon flux.

widely used to study observational data sets subject to truncation and censorship (e.g., Dainotti, Singal, Ostrowski, et al., 2013; Kocevski and Liang, 2006; Singal, Petrosian, Lawrence, et al., 2011).

Yu et al. (2015) (hereafter Y15), Petrosian, Kitanidis, and Kocevski (2015) (hereafter P15), and Lloyd-Ronning, Aykutalp, and Johnson (2019) (hereafter L19) use the method of Efron-Petrosian to deduce the local (redshift-decorrelated) luminosity function $\psi(L_0)$ and cosmic GRB formation rate $\rho(z)$ to infer that local GRBs $(z < 1)$ are in excess of the SFR. Pescalli et al. (2016) (hereafter P16) follows the same approach as the previous three, however, does not find an excess of GRBs relative to the SFR at low redshifts. Tsvetkova et al. (2017) (hereafter T17) simply deduces the luminosity function and GRB formation rate.

In this work, we hypothesize and provide evidence that the effects of detection threshold in the aforementioned studies might have been significantly underestimated. This underestimation of the detector threshold results in an artificial correlation between the luminosity/energetics of LGRBs and redshifts. This could, in turn, lead to the conclusion that the GRB formation rate is different from the SFR at any redshift.

This paper is organized as follows. Section 2.2 details the methodology used by the aforementioned papers to deduce luminosity/energy evolution $L(z)/E(z)$ given a sample of GRBs, which leads to $\psi(L_0)$ and $\rho(z)$. Section 2.3 is a reanalysis of their work (with the exception of P15, for whom we could not locate their data). Section 2.4 describes our own Monte Carlo simulation of a synthetic population of LGRBs. Finally, section 2.5 is a discussion of the results of our reanalysis and the implications of our Monte Carlo simulations.

2.2 Methods

It is often the case in the analysis of astronomical data that one is faced with reconstructing the joint bivariate or multivariate distributions from truncated data. Truncation can be due to a multitude of factors, most importantly, the Malmquist-types of biases in the population studies of GRBs (e.g., Band and Preece, 2005; Butler, Bloom, and Poznanski, 2010; Shahmoradi, 2013a; Shahmoradi and Nemiroff, 2009; Shahmoradi and Nemiroff, 2011b, 2015). The GRB luminosity and redshift distribution (L, z) is one such set of bivariate data. For simplicity, it is often assumed that the functional form of the total Luminosity Function is separable in the following form,

$$\Psi(z, L) = \rho(z)\psi(L) \tag{2.1}$$

where $\rho(z)$ is the GRB Formation Rate and $\psi(L)$ is the Luminosity Function. Efron and Petrosian (1992) developed a nonparametric technique for estimating $\rho(z)$ and $\psi(L)$ based on the c^- method of Lynden-Bell (1971). Luminosity is assumed to have a simple power law redshift dependence:

$$L(z) = g(z)L_0 = (1+z)^{\alpha}L_0 \tag{2.2}$$

such that the resulting distribution of L_0 (the redshift de-evolved luminosity), and hence $\psi(L_0)$ (the local Luminosity Function), becomes independent of redshift.

Consider the data set seen in Figure 2.1a. Instead of dealing with the entire data set, we deal with associated sets that can be constructed independent of the truncation limit that affects the full data set. Each of these associated sets includes only the objects for a given range of luminosity and redshift. For the ith data point

in the (L, z) data set, we can define the associated set J_i as,

$$J_i = \{j | L_j > L_i, z_j < z_i^{max}\} \, , \tag{2.3}$$

that is, the set of all points j given the above two conditions, where L_j is the luminosity of point j, L_i is the luminosity of the given point i, z_j is the redshift of point j, and z_i^{max} is the maximum redshift at which a GRB with luminosity L_i can be observed due to the detector threshold limit. This produces the dashed black bounding box seen in Figure 2.1a. N_i represents the number of GRBs in this region: $N_i \equiv$ size of$\{J_i\}$. This is the same as in the c^- method in Lynden-Bell (1971). R_i is the number of events that have redshift z_j less than z_i,

$$R_i \equiv \text{size of} \{j \in J_i | z_j < z_i\} \, . \tag{2.4}$$

We expect the rank R_i of z_i to be uniformly distributed between 1 and N_i if L and z are independent of each other (Efron and Petrosian, 1992). The Efron-Petrosian test statistic τ is then,

$$\tau \equiv \frac{\sum_i (R_i - E_i)}{\sqrt{\sum_i V_i}} \, , \tag{2.5}$$

where $E_i = (1 + N_i)/2$, $V_i = (N_i^2 - 1)/12$ are the expected mean and the variance of R_i, respectively. This is a specialized version of Kendell's τ statistic. The τ statistic represents the significance of the correlation in the bivariate distribution of the two quantities of interest by taking into account the effects of data truncation created by a detection threshold hard cutoff. It is normally distributed about a mean of 0 with a standard deviation of 1 (Efron and Petrosian, 1992). Hence, a τ of 2 implies a 2σ correlation. Once a correlation has been hypothesized, one simply parameterizes it in some way to remove the correlation. As has been aforementioned, a functional form of $L_0 = L_{iso}/g(z)$ has been chosen in

the majority of previous studies, where $g(z)$ has a simple power law dependence on z, $g(z) = (1+z)^{\alpha}$. Next, α is varied and L_0 is computed, which along with $(1+z)$ constitutes a new data set. Then the τ statistic is computed on each of these sets corresponding to different α values used. The one where the τ statistic is zero indicates the α parameter that removes the correlation between L_0 and z and gives the power law exponent for $g(z)$ that fully decorrelates L_{iso} and z.

Prior to constructing the τ statistic, the detector threshold limit needs to be rendered on the L_{iso} or E_{iso} graph. The following transforms a flux (P_{bol}) or fluence (S_{bol}) into L_{iso} or E_{iso}, respectively:

$$\begin{aligned} L_{iso} &= 4\pi \times d_L(z)^2 \times P_{bol} \\ E_{iso} &= 4\pi \times d_L(z)^2 \times \frac{S_{bol}}{1+z} \\ d_L(z) &= \frac{c}{H_0}(1+z)\int_0^z [(1+z')^3\Omega_M + \Omega_\Lambda]^{-1/2}\, dz' \end{aligned} \tag{2.6}$$

where F_{min} is substituted for P_{bol} or S_{bol} and $d_L(z)$ represents the distance in cm assuming concordance cosmology. For the sake of computational efficiency, an approximation to the above integral is used, as discussed in Wickramasinghe and Ukwatta (2010). It is shown to be highly accurate for a wide range of redshifts corresponding to $(1+z) > 1.1$. In this work we use the following cosmological parameters: $H_0 = 71$ [$km\ s^{-1}\ Mpc^{-1}$], $\Omega_M = 0.3$, $\Omega_\Lambda = 0.7$ (e.g., Shahmoradi and Nemiroff, 2011b).

2.3 Reanalyses of past work

In the following subsections, we attempt to regenerate and reanalyze the findings of several recent papers that present evidence in favor of a strong evolution of the GRB luminosity/energetics with redshift.

	Y15 Values	Reanalysis Values
α	$2.43^{+0.41}_{-0.38}$	$2.04^{+0.36}_{-0.37}$
τ	4.7σ	5.18σ
F_{min}	2.0×10^{-8} [$erg\ cm^{-2}\ s^{-1}$]	2.00×10^{-8} [$erg\ cm^{-2}\ s^{-1}$]

Table 2.1: Using the same value as Y15 for F_{min} yields quantitatively similar α and τ values.

2.3.1 Yu et al. (2015) (Y15)

In their paper, Y15 find an excess of LGRBs at low redshift ($z < 1$), deviating from the SFR. They use the method of Efron and Petrosian (1992) to infer the luminosity function and the cosmic rates of LGRBs based on the observational data collected by *Swift*'s Burst Alert Telescope (BAT) gamma-ray detector. They find that the luminosity function of LGRBs evolves with redshift as Eq. (2.2) with $\alpha = 2.43^{+0.41}_{-0.38}$. This conclusion is based on the assumption of a flux lower limit of

$$F_{min} = 2.0 \times 10^{-8}\ [\ erg\ cm^{-2}\ s^{-1}\ ]\ , \tag{2.7}$$

representing the detector threshold limit of *Swift*'s BAT.

To better understand the role of *Swift*'s BAT detector threshold on the conclusions drawn by Y15, here we attempt to reproduce their analysis of *Swift* data. Figures 2.1a - 2.1c depict the distributions of the observational LGRB sample used in Table 1 of Y15. Specifically, the bivariate distribution of the 1-second total isotropic peak flux (L_{iso}) and the redshifts ($1 + z$) of LGRBs as shown in plot 2.1a exhibits an apparently strong correlation. However, much of this correlation is potentially due to the BAT detection threshold effects on the observational sample of LGRBs. To quantify and eliminate the effects of detector threshold, Y15 use the proposed non-parametric methodology of Efron and Petrosian (1992) by assuming a parametrization as seen in Eq. (2.2) for the luminosity-redshift dependence in the LGRB data, such that the resulting distribution of L_0 becomes

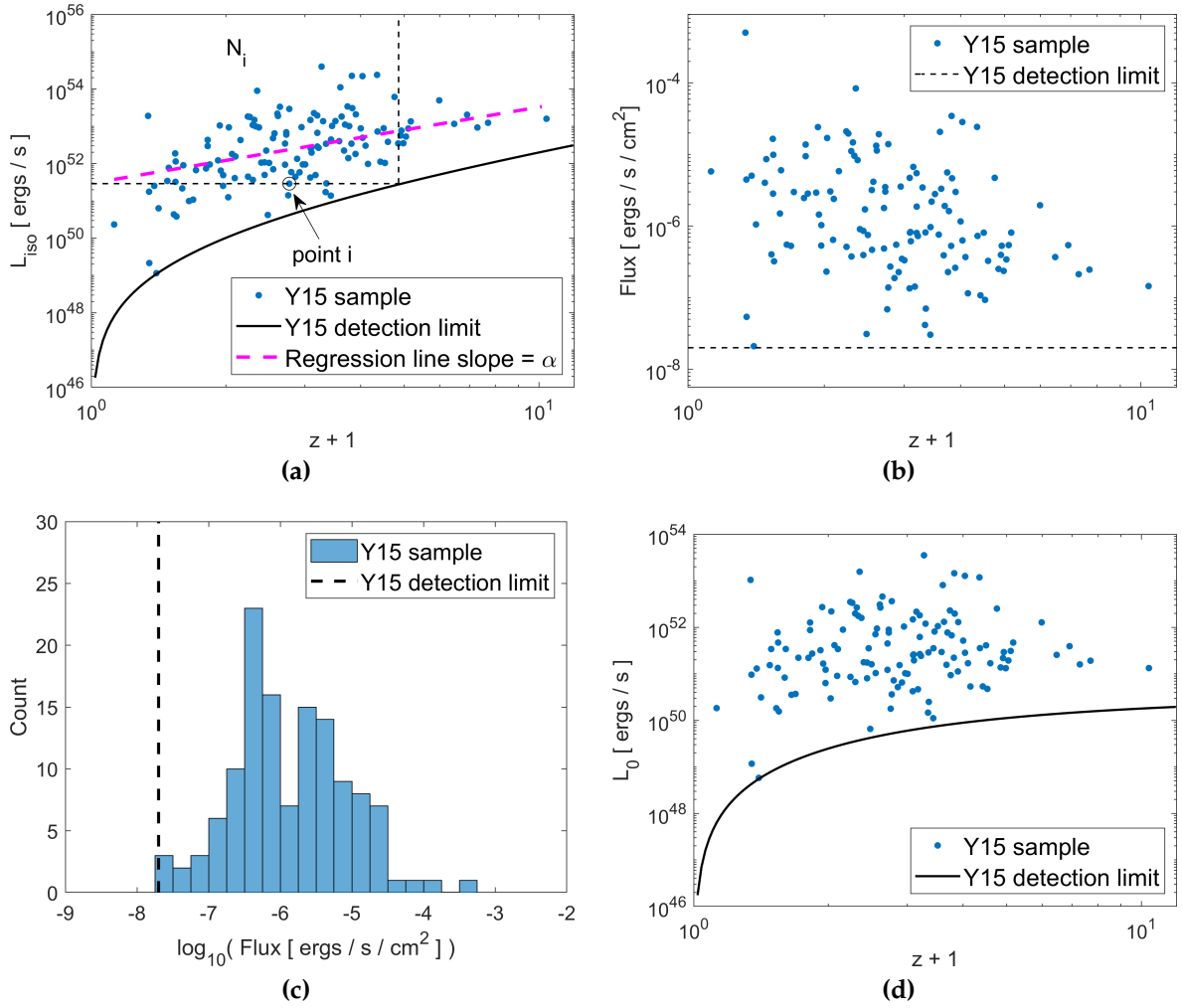

Figure 2.1: Plotting of the 127 GRBs from Y15. Plot **(a)** shows isotropic luminosity vs. redshift. The black line represents the observational limit of *Swift* assumed by Y15 to be 2.00×10^{-8} [$erg\ cm^{-2}\ s^{-1}$]. The purple line represents the linear regression through the data set whose slope is $\alpha = 2.04$. Plot **(b)** is the observer frame visualization of the Y15 data set, where the dashed line is the observational limit of Y15. Plot **(c)** is a histogram of flux, where the dashed line is the observational limit. Plot **(d)** shows redshift vs. $L_0 = L(z)/(1+z)^{2.04}$, the redshift-independent luminosity.

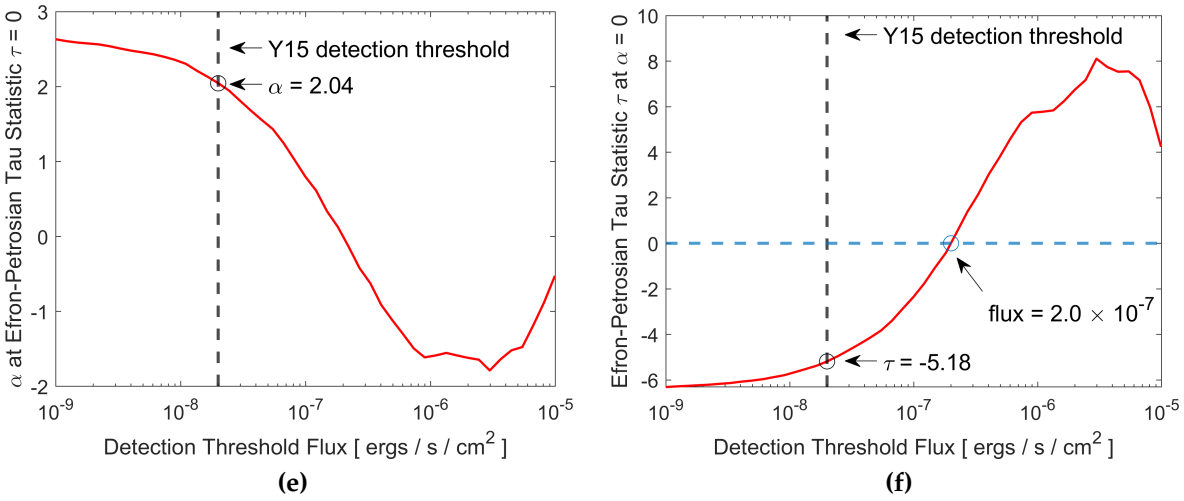

Figure 2.1: (cont.) Plot **(e)** shows a range of possible threshold limits vs. α values at $\tau = 0$. The intersection of this line with Y15's threshold limit is our value for their α. Plot **(f)** shows a range of possible threshold limits vs τ values at $\alpha = 0$. Assuming the detection threshold of Y15, a redshift-independent luminosity distribution is rejected at $|\tau| = 5.18\sigma$. However, choosing a more conservative detection threshold at 2.00×10^{-7} [$erg\ cm^{-2}\ s^{-1}$] yields no evidence for luminosity-redshift evolution.

independent of redshift. We note an apparent inconsistency between Eq. (2.5) that we have extracted from Efron and Petrosian (1992) and Eq. (9) of Y15, where summations are taken in different places.

The value of exponent that we infer from the data set of Y15 is consistent with, although not the same as, their inferred α exponent. Y15 found a value of $\alpha = 2.43^{+0.41}_{-0.38}$ in their analysis. In our reanalysis of their work, we find a value of $\alpha = 2.04^{+0.36}_{-0.37}$. However we do believe that their assumption for the value of the flux lower limit of Eq. (2.7) is likely a severe underestimation of the detection threshold of *Swift*'s BAT. In reality the detection threshold limit of the BAT detector is far more complex than a simple hard cutoff, but rather, a fuzzy range arising from a multitude of factors.

The *Swift* satellite is very well known for its immensely complex triggering algorithm. To our knowledge, it is comprised of at least three separate detection

mechanisms that complement each other (e.g., Fenimore et al., 2003):

1. The first type of trigger is for short time scales (4 ms to 64 ms). These are traditional triggers (single background), for which about 25,000 combinations of time-energy-focal plane subregions are checked per second.

2. The second type of trigger is similar to HETE: fits multiple background regions to remove trends for time scales between 64 ms and 64 s. About 500 combinations for these triggering mechanisms are checked per second. For these rate triggers, false triggers and variable non-GRB sources are also rejected by requiring a new source to be present in an image.

3. The third type of trigger works on longer time scales (minutes) and is based on routine images that are made of the field of view.

The entire complexity of the detection mechanism of *Swift*'s BAT, as mentioned above, is summarized in a single value, Eq. (2.7), in the work of Y15. The consequences of choosing this value is most apparent in Figures 2.1b and 2.1c, where the data set of detected LGRBs virtually ends before reaching the detection threshold line. This implies that the observational LGRB data set is not constrained by the assumed detection threshold of Y15, which is counterintuitive. We *do* expect the threshold to soft-truncate the data set, and this truncation likely occurs closer to the central peak of the histogram of Figure 2.1c.

This severe underestimation of the detection threshold of BAT by Y15 is very well seen in Figure 2.1d where we plot the redshift-corrected isotropic peak luminosity vs. redshift. The solid black line in this plot represents the redshift-corrected detection threshold. In agreement with our hypothesis in the previous paragraph, we observe that the resulting redshift-corrected detection threshold of Y15 resembles almost a flat line at high redshifts. This is another indication

that the inferred relationship between $(1+z)$ and L_{iso} is likely heavily influenced by the improperly-modeled detection threshold of BAT.

In Figures 2.1e and 2.1f the calculation of α and τ are taken a step further, this time by varying the detector threshold limit, F_{min}. Figure 2.1e depicts how α varies with detector threshold when τ equals zero, while Figure 2.1f depicts how τ varies with detector threshold when α equals zero. Both plots can therefore show for what value of detector threshold **both** α and τ equal zero (indicating zero correlation between L_{iso} and z), however, this is only highlighted in Figure 2.1f with the blue dashed line. In other words, how a more conservative choice of detector threshold can remove the calculated correlation entirely. For the Y15 data set, it takes only one order of magnitude to fully remove the correlation.

To gain a better insight into the effects of detection threshold on observational data, we have reproduced parts of the results of Shahmoradi and Nemiroff (2015) in Figure 2.2. This figure illustrates well the subtle fuzzy effects of the BATSE detector threshold on the observed distribution of the energetics of BATSE LGRBs and SGRBs, including the observed peak flux distribution for which a sharp detection threshold cutoff is frequently assumed. The detection threshold causes a deviation in the observed data from the inferred underlying population, to begin just to the right of the histogram peak (the solid lines). This deviation becomes more significant as one moves leftward. Y15 chose their detector threshold to begin far to the left of the histogram peak, when in reality, it should have been chosen close to the peak. If their choice of detector threshold is taken seriously, then its implications are profound: there is a suspicious lack of faint LGRBs in the universe that are *not* the result of detector threshold cutoff, or Malmquist bias. This is why the cutoff must be closer to the central peak.

Finally, we turn our attention to Y15's Monte Carlo simulations, which seemingly confirms their results. Therein, they begin with their inferred value of

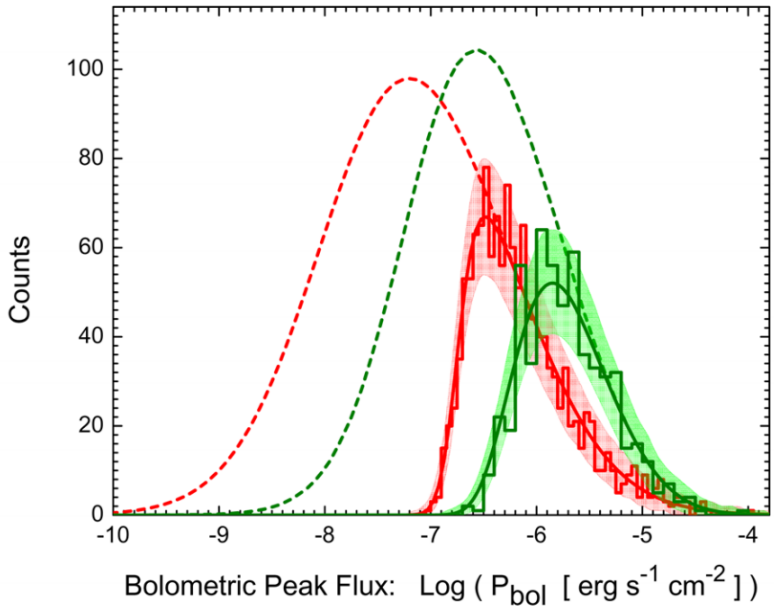

Figure 2.2: The red and green colors represent data and model for LGRBs and SGRBs, respectively, for BATSE catalogue GRBs. The solid curves illustrate the projection of the multivariate GRB world models of Shahmoradi (2013a) and Shahmoradi and Nemiroff (2015) on the BATSE-catalog peak flux P_{bol} distribution, subject to the BATSE detection threshold. The colour-shaded areas represent the 90 percent prediction intervals for the distribution of BATSE data. The dashed lines represent the predicted underlying populations of LGRBs and SGRBs, respectively based on the multivariate GRB world models of Shahmoradi (2013a) and Shahmoradi and Nemiroff (2015).

α to simulate a distribution of LGRBs following the relationship of Eq. (2.2) with $\alpha = 2.43$. They find that the synthetic data and the observed data have similar distributions. This is, however, no surprise considering their simulation was based on the derived results of their observational analysis and the assumed potentially-underestimated detection threshold. In other words, their Monte Carlo simulation proves the self-consistency of the Efron-Petrosian statistic and their analysis, but falls short of verifying the accuracy of the detection threshold assumption made in their analysis. Therefore, this circular reasoning concludes that the two observed and synthetic distributions are similar without validating the accuracies of the assumptions made in their work.

The primary conclusion of Y15, of an excess of GRBs at low redshift ($z < 1$) compared to the SFR, also contradicts previous studies based on the properties of GRB host galaxies. In point of fact, Vergani et al. (2015), Perley et al. (2015, 2016a) and Perley et al. (2016b), Krühler et al. (2015), and Schulze et al. (2015) performed spectroscopic and multi-wavelength studies on the properties (stellar masses, luminosities, SFR, and metallicity) of GRB host galaxies of various complete GRB samples and compared them to those of the star-forming galaxies selected by galaxy surveys. Their collective results indicate that at low redshift ($z < 1$) only a small fraction of the star formation produces GRBs Pescalli et al. (2016).

2.3.2 Pescalli et al. (2016) (P16)

P16 proceeds in a similar fashion to Y15, beginning with the observational data set of LGRBs found in their Table B.1. We extract from this data set 81 LGRBs that have both redshift and isotropic peak luminosity (L_{iso}) values for our reanalysis. They use the Efron-Petrosian τ statistic to find an α value of $\alpha = 2.5$, consistent with the results of Y15. This provides the functional form of the lumi-

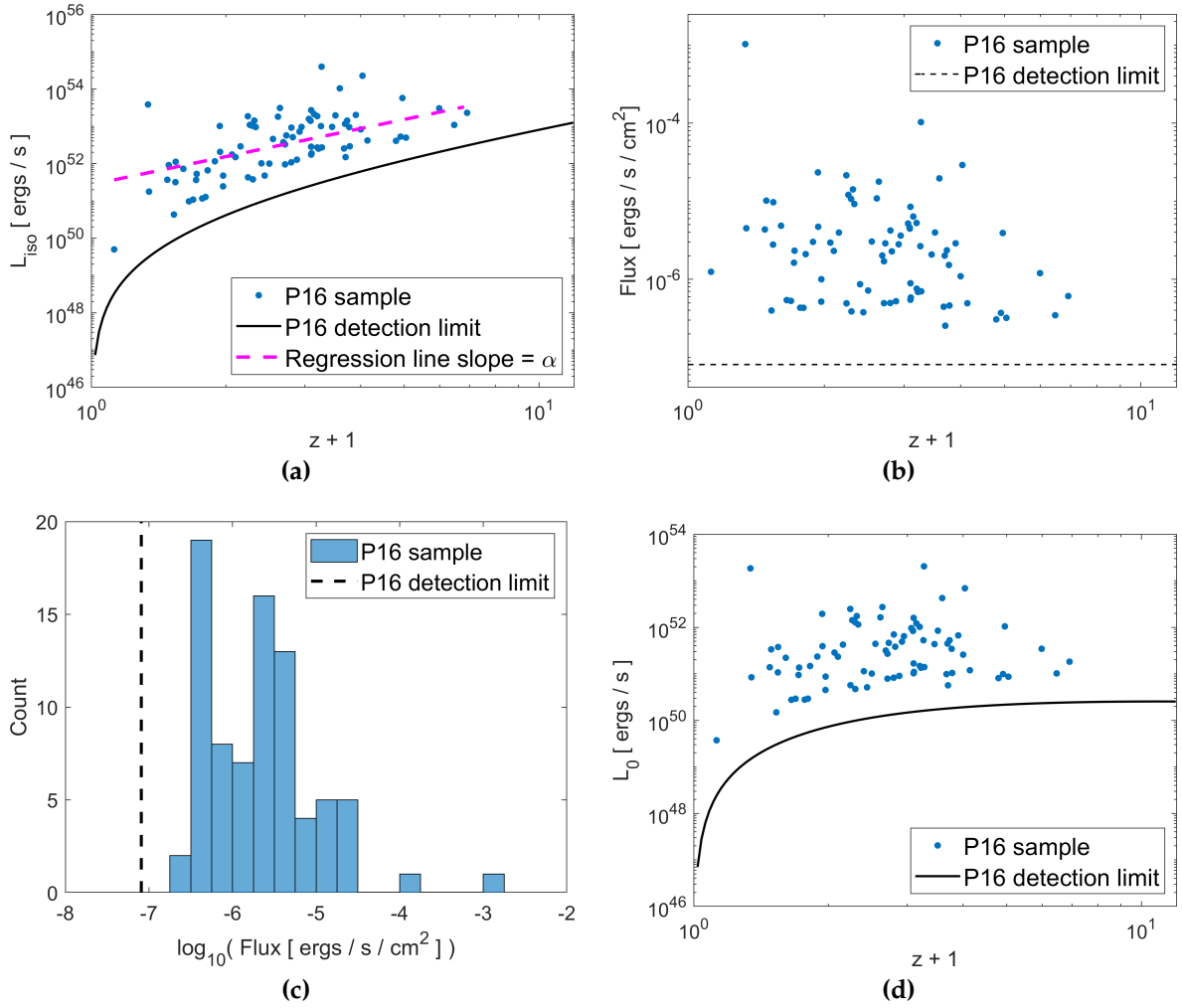

Figure 2.3: Plotting of the 81 GRBs from P16. Plot **(a)** shows redshift vs. isotropic luminosity. The black line represents the observational limit of *Swift*, which has been deduced from P16 to be 8.10×10^{-8} [$erg\ cm^{-2}\ s^{-1}$]. The purple line represents the linear regression through the data set whose slope is $\alpha = 2.50$. Plot **(b)** is the observer frame visualization of the P16 data set, where the dashed line is the observational limit. Plot **(c)** is a histogram of flux, where the dashed line is the observational limit. Plot **(d)** shows redshift vs. $L_0 = L(z)/(1+z)^{2.50}$, the redshift-independent luminosity.

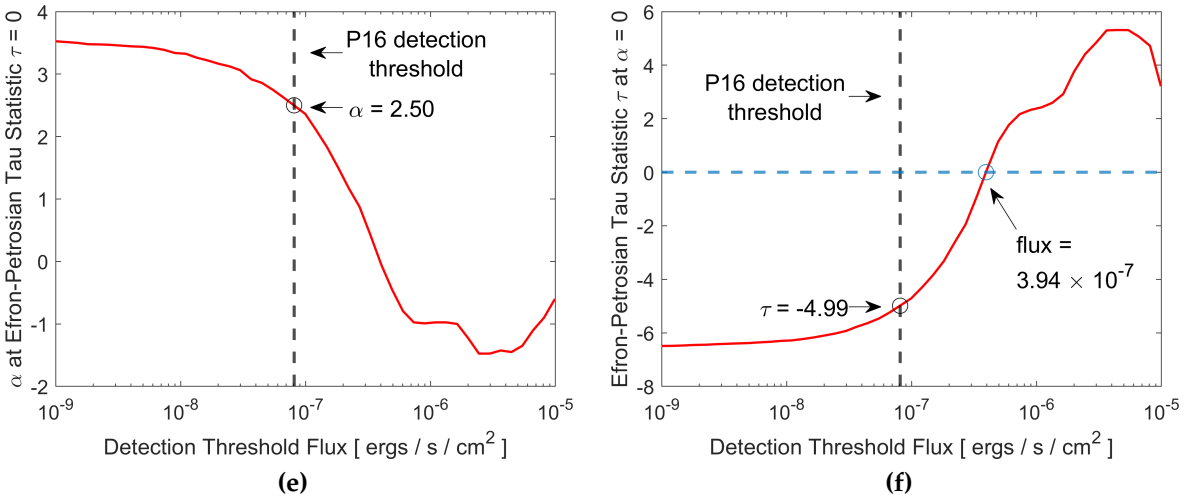

Figure 2.3: (cont.) Plot **(e)** shows a range of possible threshold limits vs. α values at $\tau = 0$. The intersection of this line with P16's supposed threshold limit is our value for their α. Plot **(f)** shows a range of possible threshold limits vs τ values at $\alpha = 0$. Assuming the detection threshold inferred from the analysis of P16, a redshift-independent luminosity distribution is rejected at $|\tau| = 4.99\sigma$. However, choosing a more conservative detection threshold at 3.94×10^{-7} [$erg\ cm^{-2}\ s^{-1}$] yields no evidence for luminosity-redshift evolution.

nosity evolution with redshift $L(z) = L_0(1+z)^{2.5}$. From here they proceed with Lynden-Bell's c^- method to derive the cumulative luminosity function $\Phi(L_0)$ and the LGRB formation rate $\rho(z)$.

These results, however, are predicated on a value of detector threshold which P16 gives as,

$$P_{lim} = 2.6\ [\ photons\ cm^{-2}\ s^{-1}\ ]\ . \tag{2.8}$$

This corresponds to an instrument that is $\sim$6 times less sensitive than *Swift*'s BAT (Salvaterra et al., 2012). In their work, P16 adopt a slightly different approach to modeling the flux limit of their sample. The quantities L_{lim} and z_{max} that are used in the Efron-Petrosian statistic are computed by adopting individual spectral and temporal properties of LGRBs and applying the corresponding K-corrections. This approach results in a small scatter in the energy flux-limit of their $L_{iso} - (1+z)$ plane. However, they find that this non-uniqueness of the

	P16 Values	Reanalysis Values
α	2.5	$2.50^{+0.40}_{-0.44}$
τ	Not given	4.99σ
F_{min}	Given as P_{lim}	8.10×10^{-8} [$erg\ cm^{-2}\ s^{-1}$]

Table 2.2: A value for F_{min} was chosen such that the resulting α value matches P16's value. Using a Band model with P_{lim} was unsuccessful.

detection threshold has a very small impact in the computation of their τ statistic.

Given the lack of sufficient details about the approach proposed by P16 and the fact they find almost no difference between the traditional approach to computing the Efron-Petrosian statistic and their proposed method, here we follow the traditional formal technique for computing the τ statistic. However, since P16 do not provide an effective bolometric energy flux limit for their sample in units of [$erg\ cm^{-2}\ s^{-1}$], we searched for an effective energy flux detection threshold that would yield a τ statistic comparable to what P16 find.

We find that an effective detection threshold of $F_{min} = 8.10 \times 10^{-8}$ [$erg\ cm^{-2}\ s^{-1}$] yields a regression slope of $L_{iso} - (1+z)$ correlation of $\alpha = 2.50^{+0.40}_{-0.44}$ which is identical to the reported value by P16. Alternatively, we also compute the corresponding detection threshold energy flux by converting the photon flux threshold of Eq. (2.8) to an effective energy flux limit by assuming a Band model (Band et al., 1993) of the form,

$$\Phi(E) \propto \begin{cases} E^{\alpha_{ph}}\ \mathrm{e}^{\left(-\frac{(2+\alpha_{ph})E}{E_p}\right)} & \text{if } E \leq \left(E_p\right)\left(\frac{\alpha_{ph}-\beta_{ph}}{2+\alpha_{ph}}\right), \\ E^{\beta_{ph}} & \text{if otherwise.} \end{cases} \tag{2.9}$$

with low- and high-energy spectral indices of $\alpha_{ph} = -1$ and $\beta_{ph} = -2.25$, respectively, taken from Salvaterra et al. (2012) and an effective spectral peak energy fixed to the average observed spectral peak energy of the LGRB sample of P16 ($E_p = 574\ keV$). Using this approach, we obtain an effective energy flux limit

($F_{min} = 2.34 \times 10^{-7}$ [$erg\ cm^{-2}\ s^{-1}$]) for the LGRB sample that results in a completely different value, $\alpha = 1.35^{+0.50}_{-0.45}$, for the regression slope of the $L_{iso} - (1+z)$ relation than what is reported by P16.

Therefore, we conclude that the effective detection threshold ($F_{min} = 8.10 \times 10^{-8}$ [$erg\ cm^{-2}\ s^{-1}$]) that we previously inferred directly from the Efron-Petrosian statistic should likely resemble more the flux limit that is used but not clearly discussed or shown in the work of P16. However, the trade off in choosing this value is that the limit appears to be underestimated, as can be seen in Figures 2.3a - 2.3c. It is not possible to choose a value of E_p that both yields an α value in agreement with P16 *and* does not appear to underestimate the detector threshold flux limit.

Assuming this chosen value for F_{min} is indeed an appropriate approximation for that used by P16, we are again faced with an underestimation of the true effective value of the detection threshold of *Swift*, similar to Y15. This can be clearly seen in Figure 2.3d where we plot the redshift-corrected isotropic peak luminosity vs. redshift, and the solid black line represents the redshift-corrected detection threshold. We observe that this threshold resembles almost a flat line at high redshifts, indicating that the inferred relationship between $(1+z)$ and L_{iso} is likely heavily influenced by the improperly-modeled detection threshold of BAT. In Figure 2.3f it can be seen that the reported correlation can be removed entirely with a more conservative value of $F_{min} = 3.94 \times 10^{-7}$ [$erg\ cm^{-2}\ s^{-1}$].

In addition to potential underestimation of the detection threshold, the observational data in the work of P16 also appears to not have been homogeneously collected. Looking at Figure 2.3c, the histogram of data appears to be multi-modal/incomplete, implying the presence of some, yet-unknown, selection effects in the process of constructing this data set.

Finally, we turn our attention to P16's Monte Carlo simulation, which seems

	T17 Values	Reanalysis Values
α	1.7	$1.70^{+0.34}_{-0.26}$
τ	1.2σ	5.46σ
F_{min}	2×10^{-6} [$erg\ cm^{-2}\ s^{-1}$]	7.95×10^{-7} [$erg\ cm^{-2}\ s^{-1}$]

Table 2.3: Using T17's value for F_{min} does not reproduce their α value, so an F_{min} was chosen that does.

to confirm their results. Unlike Y15, P16 avoid a circular logic inference in their simulations by assuming different F_{min} (5×10^{-8} [$erg\ cm^{-2}\ s^{-1}$]) and α (2.2) values from their methodology and results. They are able to successfully recover the GRB formation rate and luminosity function that they adopted for their simulated sample.

They further test the consequences of sample incompleteness in two approaches. In the first approach they randomly remove a fraction of the bursts close to F_{min}. In the second approach, they lower F_{min} by a factor of 5, creating an underestimation of its value. Both approaches artificially create sample incompleteness. The result of both realizations of sample incompleteness is to flatten out the GRB formation rate at low redshift, creating the illusion of an excess of low-redshift GRBs relative to the SFR. This result contradicts the simulations and findings of Y15 and corroborates our conclusions in §2.3.1.

2.3.3 Tsvetkova et al. (2017) (T17)

In T17, the authors explore a data set of GRBs detected in the triggered mode of the Konus-*Wind* experiment. Beginning with 150 mixed-type GRBs, they prune the data set down to 137 by removing the Type I (short) GRBs as well as GRB 081203A. It is not explained why GRB 081203A is excluded.

Similar to Y15 and P16, they employ the Efron-Petrosian τ statistic to find the luminosity evolution, assuming a functional form as seen in Eq. (2.2). They find

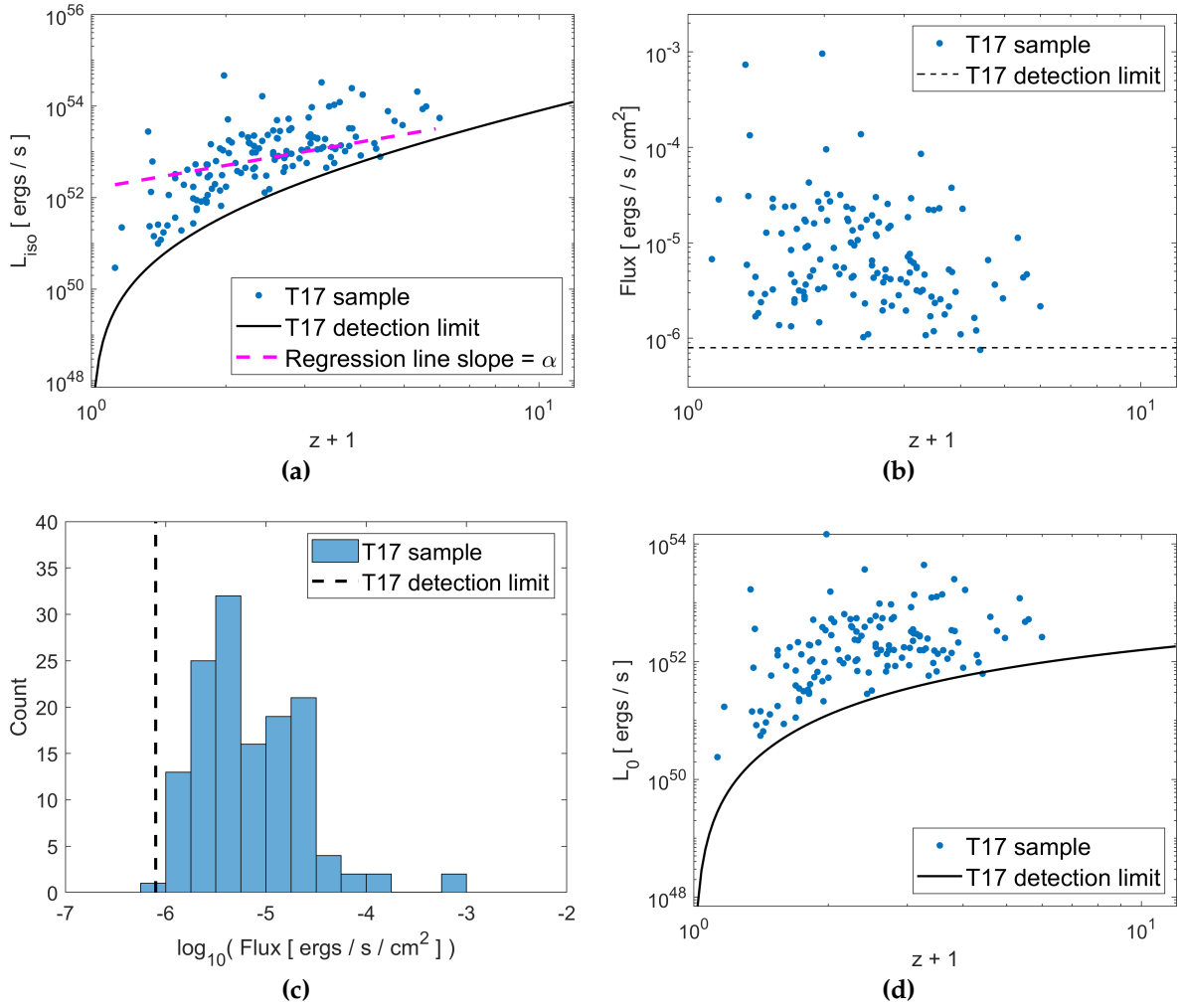

Figure 2.4: Plotting of the 137 GRBs from T17. Plot **(a)** shows redshift vs. isotropic luminosity. The black line represents the observational limit of *Swift*, which has been deduced from T17 to be 7.95×10^{-7} [$erg\ cm^{-2}\ s^{-1}$]. The purple line represents the linear regression through the data set whose slope is $\alpha = 1.70$. Plot **(b)** is the observer frame visualization of the T17 data set, where the dashed line is the observational limit. Plot **(c)** is a histogram of flux, where the dashed line is the observational limit. Plot **(d)** shows redshift vs. $L_0 = L(z)/(1+z)^{1.70}$, the redshift-independent luminosity.

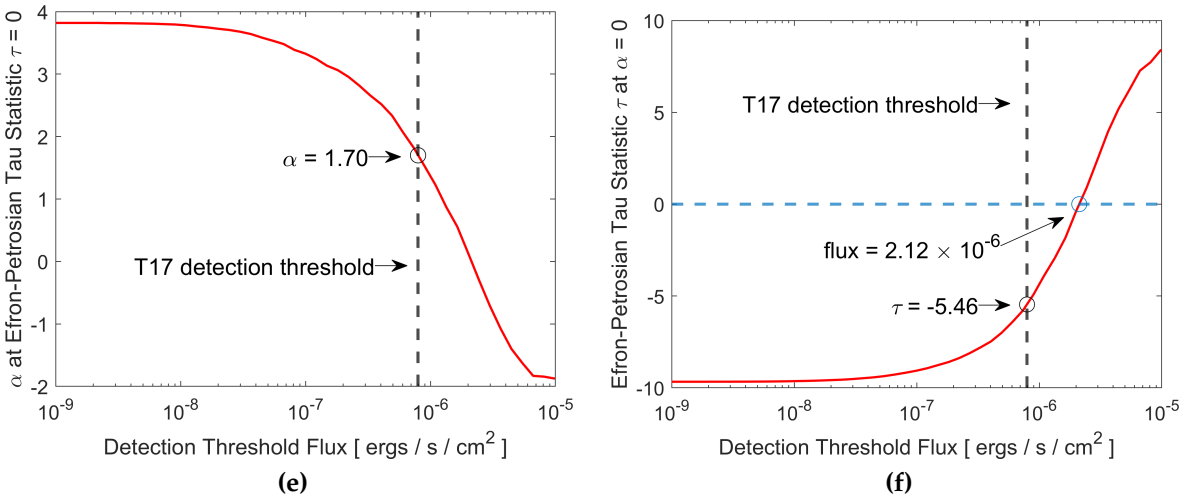

Figure 2.4: (cont.) Plot **(e)** shows a range of possible threshold limits vs. α values at $\tau = 0$. The intersection of this line with T17's supposed threshold limit is our value for their α. Plot **(f)** shows a range of possible threshold limits vs τ values at $\alpha = 0$. Assuming the detection threshold inferred from the analysis of T17, a redshift-independent luminosity distribution is rejected at $|\tau| = 5.46\sigma$. However, choosing a more conservative detection threshold at 2.12×10^{-6} [$erg\ cm^{-2}\ s^{-1}$] yields no evidence for luminosity-redshift evolution.

individual truncation limits to the $(1+z) - L_{iso}$ plane calculated for each burst separately, yielding an α value of $\alpha = 1.7$. They note that similar results were obtained by using the "monolithic" truncation limit of

$$F_{min} = 2 \times 10^{-6}\ [\ erg\ cm^{-2}\ s^{-1}\ ]\ . \tag{2.10}$$

Since both methods yield the same α value, we will use the single-valued limit, as we have in our previous analyses. When we do so, we obtain a value of $\alpha = 0.29^{+0.28}_{-0.28}$, which is significantly different from the reported value of 1.7. This should not be the case, so we turn to another method for obtaining α by visually matching the threshold cut from their Figure 8. Doing so requires a threshold of 1.1×10^{-6} [$erg\ cm^{-2}\ s^{-1}$] and yields $\alpha = 1.36^{+0.27}_{-0.34}$. Still not the reported α value, we search for the threshold limit of 7.95×10^{-7} [$erg\ cm^{-2}\ s^{-1}$] which correctly

	L19 Values	Reanalysis Values
α	2.3 ± 0.5	$1.31^{+0.21}_{-0.20}$
τ	5.6σ	6.01σ
F_{min}	2×10^{-6} [$erg\ cm^{-2}$]	1.60×10^{-7} [$erg\ cm^{-2}$]

Table 2.4: Using L19's value for F_{min} does not reproduce their α value, and a reasonable F_{min} could not be chosen that does, so instead one was deduced to visually match the threshold cut on their graph. This yields a significantly different α value, however.

yields $\alpha = 1.70^{+0.34}_{-0.26}$. This can be seen in Figures 2.4a - 2.4c.

As can be seen in Figures 2.4b and 2.4c, the analysis of T17 also appears to suffer from an underestimation of the detector threshold limit of *Swift*. Again, we expect the limit to be closer to the central peak of the histogram, soft-truncating the data set. Otherwise, such a sharp drop in the count of LGRB events before reaching the detection threshold would have truly fundamental and revolutionary implications about the cosmic rates of LGRBs.

We note that T17's underestimation of the detector threshold limit does not appear to be as severe as Y15 or P16. Once the luminosity evolution has been removed, the detector threshold cut in the $(1+z) - L_0$ plane does not become flat at high redshift, as can be seen in Figure 2.4d.

Also of note is the disparity in the significance of rejecting no luminosity-redshift evolution between our results and those of T17. Figure 2.4f shows our inferred significance ($\tau = 5.46\sigma$), which is hard to reconcile with the inferred significance $\tau = 1.2\sigma$ in T17. This figure also highlights that a more conservative value of $F_{lim} = 2.12 \times 10^{-6}$ [$erg\ cm^{-2}\ s^{-1}$] removes the apparent correlation between L_{iso} and z entirely.

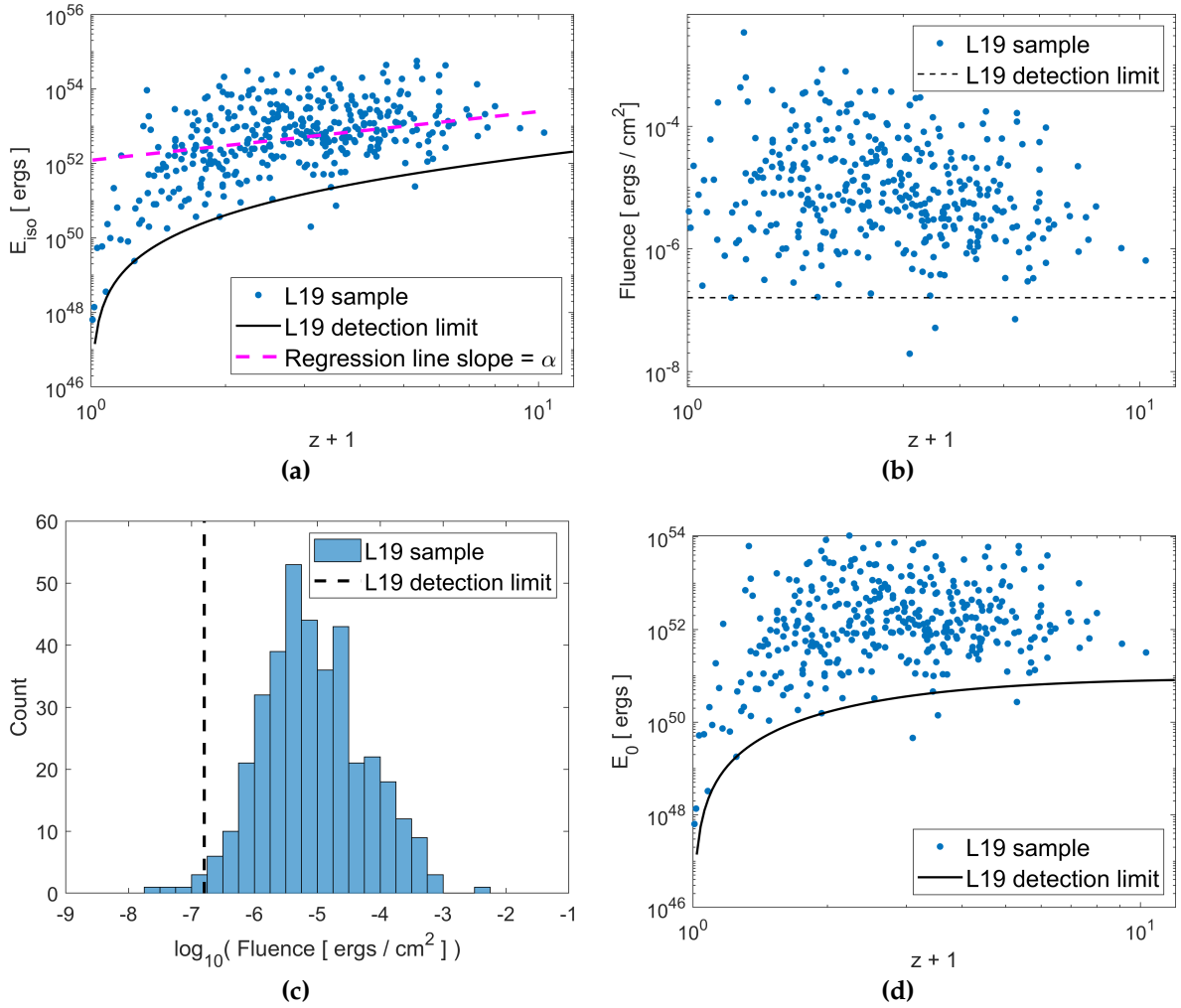

Figure 2.5: Plotting of the 376 GRBs from L19. Plot **(a)** shows redshift vs. isotropic emitted energy. The black line represents the observational limit of *Swift*, which has been deduced from L19 to be 1.60×10^{-7} [$erg\ cm^{-2}$]. The purple line represents the linear regression through the data set whose slope is $\alpha = 1.31$. Plot **(b)** is the observer frame visualization of the L19 data set, where the dashed line is the observational limit. Plot **(c)** is a histogram of fluence, where the dashed line is the observational limit. Plot **(d)** shows redshift vs. $E_0 = E(z)/(1+z)^{1.31}$, the redshift-independent effective energy.

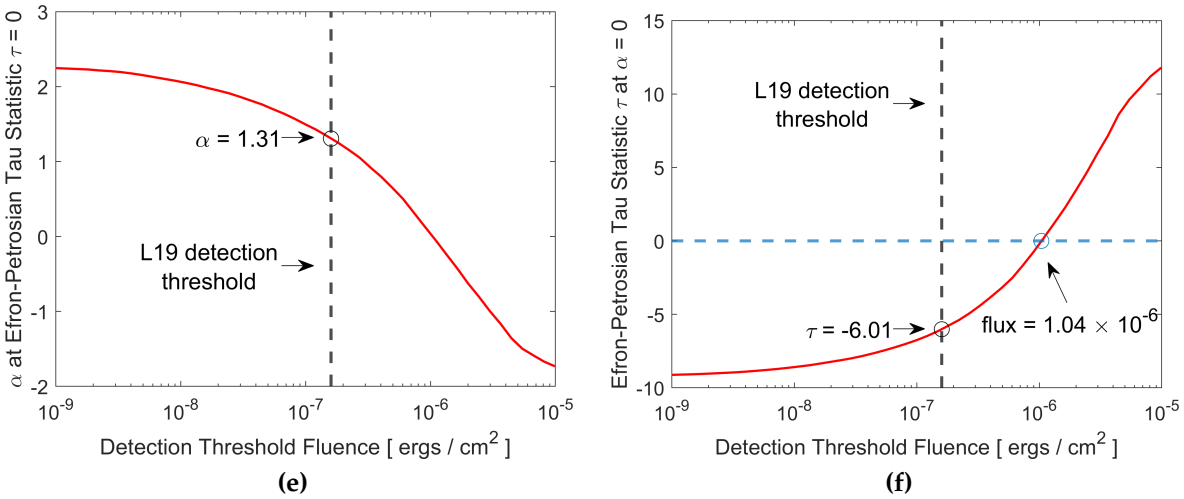

Figure 2.5: (cont.) Plot **(e)** shows a range of possible threshold limits vs. α values at $\tau = 0$. The intersection of this line with L19's supposed threshold limit is our value for their α. Plot **(f)** shows a range of possible threshold limits vs τ values at $\alpha = 0$. Assuming the detection threshold inferred from the analysis of L19, a redshift-independent luminosity distribution is rejected at $|\tau| = 6.01\sigma$. However, choosing a more conservative detection threshold at 1.04×10^{-6} [$erg\ cm^{-2}$] yields no evidence for luminosity-redshift evolution.

2.3.4 Lloyd-Ronning, Aykutalp, and Johnson (2019) (L19)

In L19, the authors use a data set taken from Wang et al. (2020) that consists of all publicly available observations of 6289 GRBs, from 1991 to 2016. They isolate those events with a measured redshift and observed duration of $T_{90} > 2s$ (LGRBs), which can yield an estimate of the total isotropic gamma-ray emission, E_{iso}. This leads to the selection of 376 LGRB events by L19, based upon which they proceed to construct the τ statistic, in similar fashion to the previous studies, to find the redshift evolution parameter, α. L19 choose a functional form of $E_{iso} = E_0(1+z)^{\alpha}$, and find that $\alpha = 2.3 \pm 0.5$. L19 report a value of,

$$F_{min} = 2 \times 10^{-6}\ [\ erg\ cm^{-2}\ ]\ . \tag{2.11}$$

used in their study. However, when we use this limit in our reanalysis, the

threshold line cuts through the majority of the data set, and yields a value of $\alpha = -0.58^{+0.18}_{-0.18}$. Our inferred value for α is completely at odds with the value reported by L19. In order to obtain their value of α, we have to use a threshold limit of 1.60×10^{-10} [$erg\ cm^{-2}$], which yields $\alpha = 2.30 \pm 0.24$. This inferred detection threshold cut is almost two orders of magnitude below the data set.

To resolve the disagreement between our inferred value of detection threshold used by L19 and the reported value in their study, we instead settle on visually matching the threshold cut in Figure 1 of L19 to obtain a limit of 1.60×10^{-7} [$erg\ cm^{-2}$]. This yields Figure 2.5a which looks remarkably similar to the corresponding Figure 1 of L19. Assuming this detection threshold, we obtain a value of $\alpha = 1.31^{+0.21}_{-0.20}$ using the Efron-Petrosian τ statistic.

If our inferred detection threshold is indeed the value used by L19 in their study, then Figures 2.5b and 2.5c, lead us to conclude that the detection threshold has been likely severely underestimated in the study of L19. The effective threshold represented by the dashed line in the histogram of Figure 2.5c is well to the left of the peak of the distribution of LGRB fluences.

Our conclusion in the above is further confirmed by Figure 2.5d, where we plot the redshift-corrected isotropic effective energy vs. redshift. The solid black line in this plot represents the redshift-corrected detection threshold and almost resembles a flat line at high redshifts. This is another indication that the inferred relationship between (1+z) and E_{iso} is likely heavily influenced by the improperly-modeled detection threshold. In this study, however, the effective threshold cut represent the combined effects of the detection thresholds of multiple satellites due to the heterogenous collection of data from multiple independent GRB catalogs. All of these raise the possibility that L19's single-valued threshold is likely a severe oversimplification of the complex merger of individual satellite thresholds, while none of the individual satellite thresholds might be well represented

by a single-valued hard cutoff.

Figure 2.5e shows a range of possible threshold limits vs. α values at $\tau = 0$. One can see the red line approaches L19's value of $\alpha = 2.3$ on the far left edge of the graph. Figure 2.5f indicates that E_{iso} and z are correlated at 6.01σ significance assuming our inferred threshold has been used by L19. Although this significance is not the same as the value reported by L19, 5.6σ, it is similar. Note, however, that this inferred detection threshold still severely underestimates the actual combined effects of multiple detection thresholds on the heterogenous data set of L19. As can be seen in the figure, a more conservative choice of $F_{min} = 1.04 \times 10^{-6}$ [$erg\ cm^{-2}$] removes the apparent correlation between E_{iso} and z entirely.

2.4 Monte Carlo Simulations of Luminosity-Redshift Evolution

To further investigate the effects of detection threshold underestimation on the inferred luminosity-redshift evolution of LGRBs, we also create a Monte Carlo universe of LGRBs. The premise of our simulation is that the LGRB world is devoid of any luminosity-redshift or energetics-redshift correlations. Therefore, the application of the Efron-Petrosian statistic on any collection of events measured from such Monte Carlo universe of LGRBs, subjected to a given simulated detection threshold, should also accurately predict no energetics/luminosity-redshift correlations for the intrinsic underlying population of LGRBs in the Monte Carlo universe.

2.4.1 The LGRB World Model

We follow the approach extensively discussed in Osborne, Shahmoradi, and Nemiroff (2020), Shahmoradi (2013a,b), Shahmoradi and Nemiroff (2015), and Shahmoradi and Nemiroff (2019), to construct our Monte Carlo Universe of LGRBs. Toward this, we assume that the intrinsic comoving rate density of LGRBs follows a piecewise power-law function of the form,

$$\dot{\zeta}(z) \propto \begin{cases} (1+z)^{\gamma_0} & z < z_0 \\ (1+z)^{\gamma_1} & z_0 < z < z_1 \\ (1+z)^{\gamma_2} & z > z_1 \,, \end{cases} \tag{2.12}$$

whose parameters,

$$(z_0, z_1, \gamma_0, \gamma_1, \gamma_2) = (0.97, 4.00, 3.14, 1.36, -2.92) \,, \tag{2.13}$$

are adopted from Butler, Bloom, and Poznanski, 2010. This SFR is henceforth referred to as the B10 rate. For simplicity, but also as argued by Osborne, Shahmoradi, and Nemiroff (2020), Shahmoradi (2013a,b), Shahmoradi and Nemiroff (2015), and Shahmoradi and Nemiroff (2019), we consider a 4-dimensional Multivariate Lognormal Probability Density Function (PDF) for the joint distribution of the four main LGRB prompt gamma-ray emission characteristics: The total isotropic peak luminosity (L_{iso}), the total gamma-ray emission (E_{iso}), the intrinsic spectral peak energy (E_{pz}), and the intrinsic duration (T_{90z}).

We use the BATSE catalog of 1366 LGRBs (Goldstein et al., 2013; Paciesas et al., 1999; Shahmoradi and Nemiroff, 2010) to construct a Bayesian hierarchical model (Shahmoradi, 2017) of the cosmic distribution of LGRBs in the universe, subject to an accurate modeling of the detection threshold of BATSE Large Area

Detectors (LADs) and data uncertainties. Then, we use a variant of the adaptive Markov Chain Monte Carlo techniques to sample the resulting posterior distribution of the parameters of the hierarchical model (Shahmoradi, 2019; Shahmoradi and Bagheri, 2020; Shahmoradi and Bagheri, 2020c; Shahmoradi, Bagheri, and Osborne, 2020). Details of model construction and sampling are extensively discussed in the aforementioned papers (e.g., Osborne, Shahmoradi, and Nemiroff, 2020; Shahmoradi, 2013a).

2.4.2 The Monte Carlo Universe of LGRBs

Once the best-fit parameters of the LGRB world model are inferred, we create a Monte Carlo Universe of LGRBs by randomly and repeatedly generating LGRB events whose characteristics are distributed according to the LGRB World model constructed in §2.4.1. For each LGRB event synthesis, we use a set of model parameters randomly drawn from the posterior distribution of the LGRB world model parameters explored in §2.4.1. Then, each LGRB passes through the simulated LGRB detection process of the BATSE LADs.

An illustration of the resulting Monte Carlo Universe of LGRBs is provided in Figure 2.6. The two plots represent the joint distributions of E_{iso}/L_{iso} and redshift. Clearly, the BATSE LADs create a rather sharp cut on the synthesized $z - L_{iso}$ sample of LGRBs compared to the distribution of $z - E_{iso}$, which exhibits much fuzzier detection threshold effects. This is expected and reassuring, since the BATSE LADs are primarily triggered on the peak photon flux at different timescales.

We note that the specific shape of the energetics or redshift distribution of LGRBs or the specific detection mechanism of LGRBs in our Monte Carlo simulations has no relevance or effects on our assessment of the utility and accuracy of the Efron-Petrosian statistic. All that is important here, is the lack of any a pri-

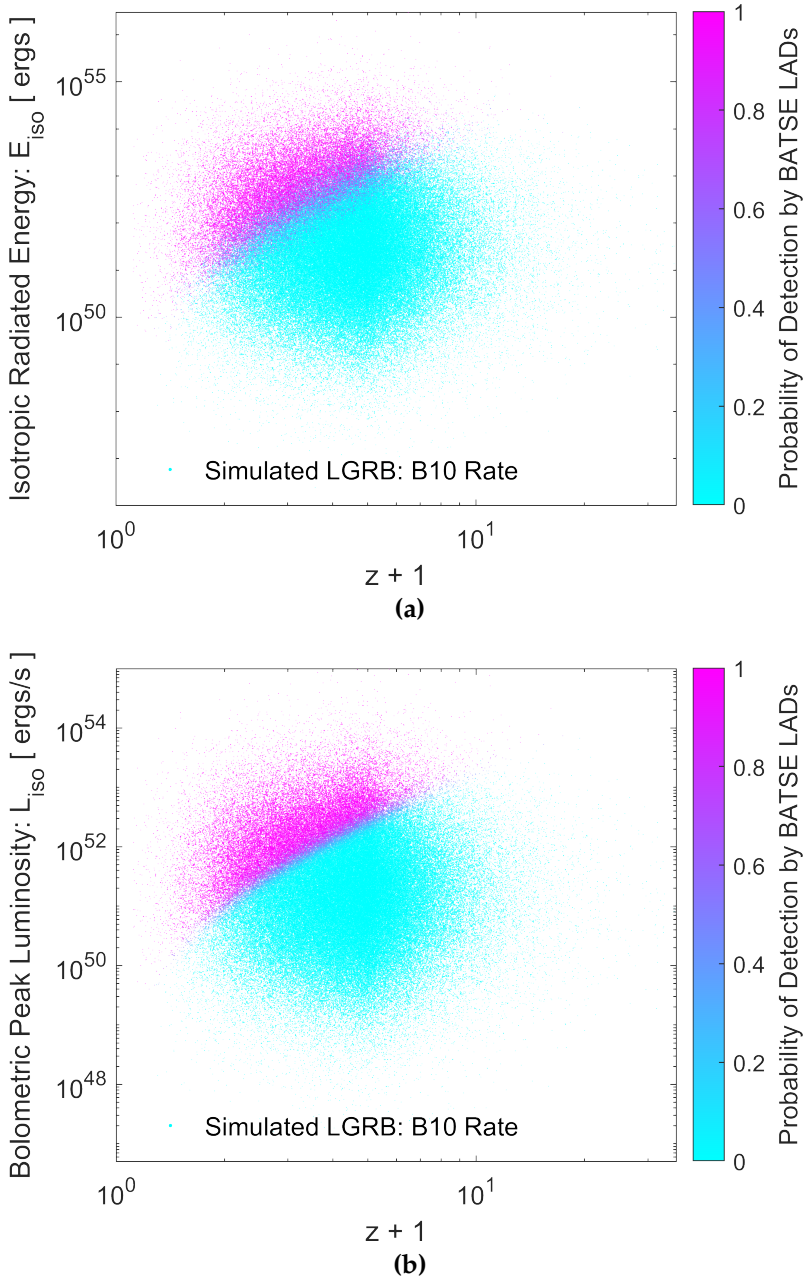

Figure 2.6: An illustration of the Monte Carlo universe of LGRBs constructed in §2.4.2 using the B10 rate. Each point in this plot represents one synthetic LGRB. The magenta color represents a high probability of detection while the cyan represents a low probability of detection.

ori correlations between the energetics and the redshifts of LGRBs in our Monte Carlo simulations.

Using our Monte Carlo universe of LGRBs, we generate a random sample of 380 BATSE-detectable LGRBs. This sample size is comparable to the size of the observational data sets collected and analyzed in previous studies. We flag an LGRB as detectable by generating a uniform-random number between 0 and 1 and comparing it to the probability of detection of the LGRB. If the probability of detection is higher than the randomly generated number, we include the event in the sample of detected LGRBs for our analysis.

2.4.3 Analysis of Synthetic Monte Carlo Data

We start with the synthetic $E_{iso} - z$ sample shown in figure 2.7a where the black line represents the BATSE detector threshold at 50% detection probability and the color on each point represents the probability of that burst being detected by BATSE. From it we take those bursts which have a probability of being detected between 48% and 52% and take the average value of the "observed" quantity in our synthetic sample for our 50% probability of detection. The corresponding lower limit on the fluence at this 50% chance of detection is

$$F_{min} = 1.88 \times 10^{-6} \, [\, ergs \; cm^{-2} \,] \, . \tag{2.14}$$

We then apply the Efron-Petrosian statistic to our synthetic data set and find that $\alpha = 0.11 \pm 0.24$ with the detection threshold set at 50% probability of detection. This is reassuring as it implies that the Efron-Petrosian test statistic remains relatively unbiased even when the detection threshold is not a sharp cutoff. But this is true only for as long as the detection threshold is not significantly underestimated.

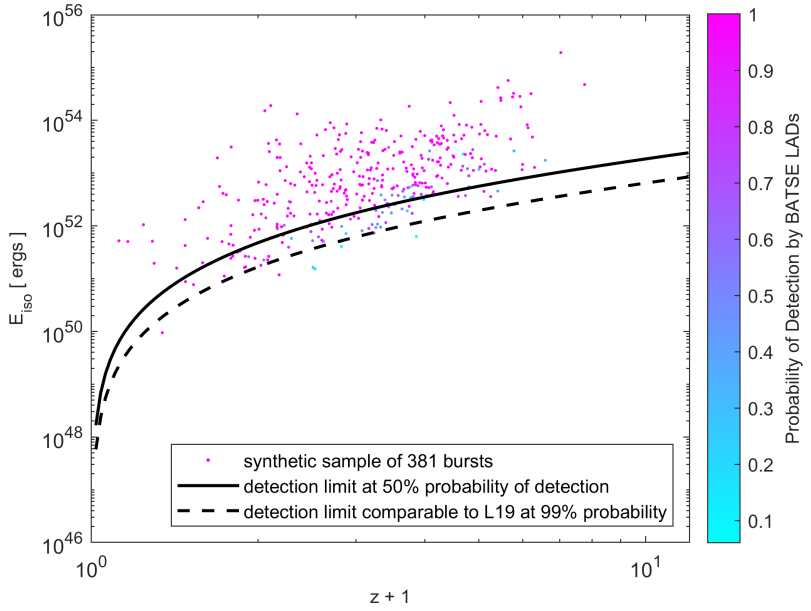

(a)

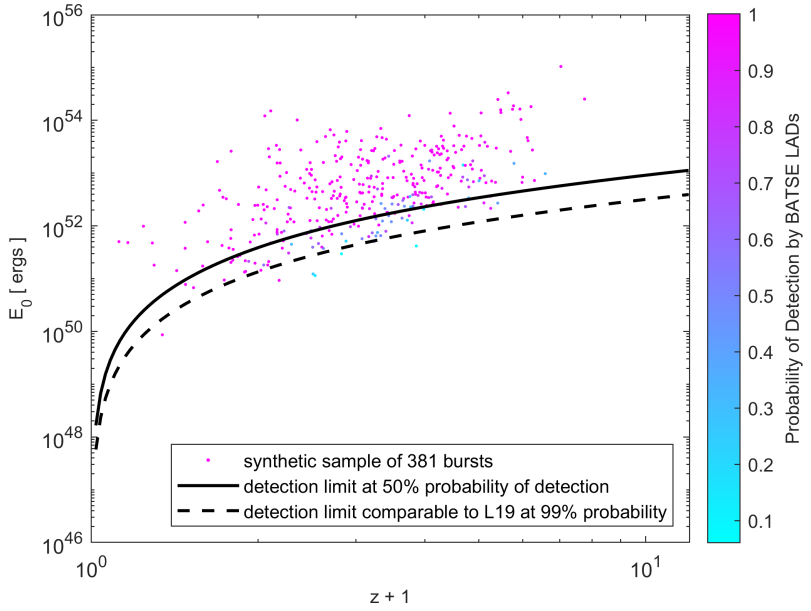

(b)

Figure 2.7: An illustration of the effects of detection threshold on the outcome of the Efron-Petrosian test statistic. Plot **(a)** Shows the synthetic data set used for our study of $(E_{iso}, 1+z)$ correlation. The solid black line represents the detector threshold at 50% while the dashed black line represents a detector threshold comparable to that of L19 at 99% probability of detection. The color bar represents the probability of detection by the BATSE LADs where cyan and magenta represent 0% and 100% chances of detection, respectively. Plot **(b)** shows the redshift-evolution corrected data set based off of the value of alpha calculated using the detector threshold at 50% probability of detection.

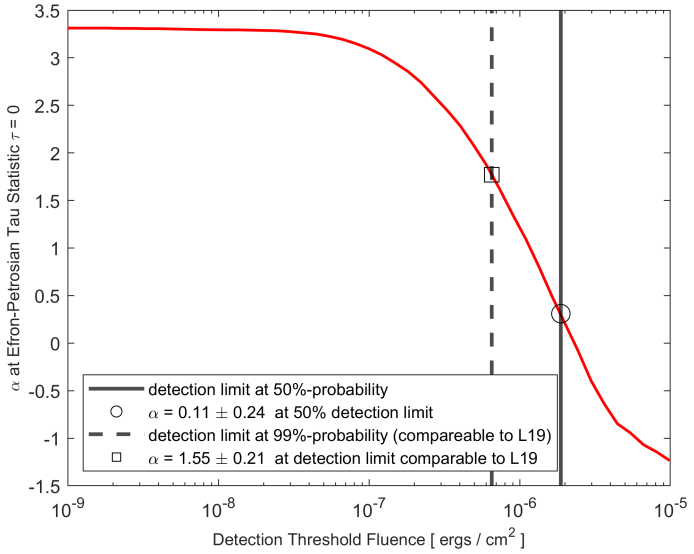

(c)

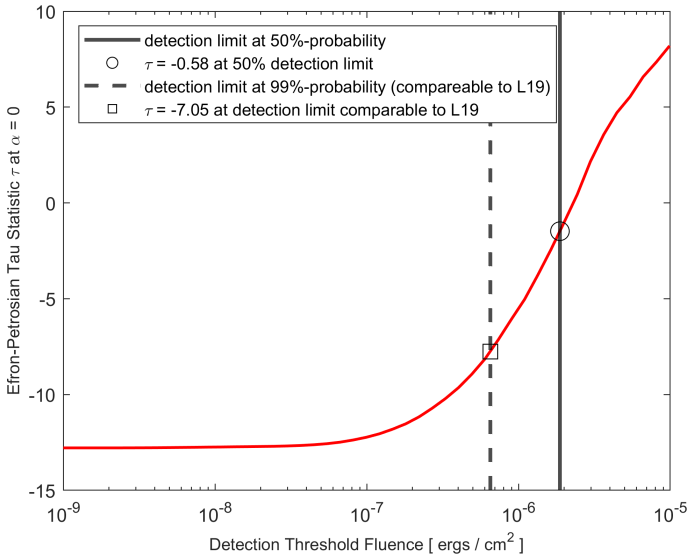

(d)

Figure 2.7: (cont.) Plot **(c)** shows the alpha value calculated corresponding to $\tau = 0$ with varying detection threshold limits. The solid black line represents the detector threshold at 50%, the black circle is the average α value over 50 generated samples for the specific threshold used, while the dashed black line represents the detector threshold at 99% probability of detection, comparable to those of previous studies, and the black square is the average α over 50 generated samples at $\tau = 0$. Plot **(d)** displays the τ statistic at $\alpha = 0$. The black line represents the detector threshold at 50% detection probability and the dashed black line represents the detection threshold at 99% detection probability, comparable to those of previous studies. The circle and square in this figure are the average τ values over 50 generated samples.

To further illustrate this, we consider a lower detection threshold, comparable to the value used in L19. We note that a direct application of the assumed detection threshold of L19 to our analysis is not possible since the data set used in L19 has been collected from multiple heterogenous sources, as opposed to our synthetic homogenously-detected LGRB sample. However, a detection threshold equivalent to that of L19 can be obtained in our analysis by noting that the detection threshold cutoff assumed in the study of L19 is above only 3 individual LGRB events. This comprises less than 1% of the entire data set of 376 LGRBs in L19.

We therefore, choose our detection threshold limit such that only 1% of our synthetic sample falls below the assumed detection threshold hard cutoff, similar to that of L19. This yields a value of $\alpha = 1.55 \pm 0.21$ which is depicted illustrated in Figure 2.7c. This inferred non-zero correlation at 7σ significance clearly contradicts the fundamental assumption of our Monte Carlo simulation, and confirms our hypothesis that an underestimation of the detection threshold can readily bias the Efron-Petrosian test statistic.

As seen in Figure 2.8, we repeat the above analysis for the joint distribution of $z - L_{iso}$ with a detection threshold hard cutoff set at 50% probability of detection: 1.88×10^{-7} [$ergs\ cm^{-2}\ s^{-1}$]. We find $\alpha = -0.04 \pm 0.24$ at this probability of detection. However, when we use a detection threshold comparable to those of Y15, P16, and T17, we find $\alpha = 1.72 \pm 0.16$ at $> 10\sigma$ significance, again contradicting the a priori assumption of our Monte Carlos universe of LGRBs.

2.5 Discussion

In this work we re-analyzed several previous studies on the evolution of the luminosity/energetics of LGRBs with redshift. To be consistent with the previous

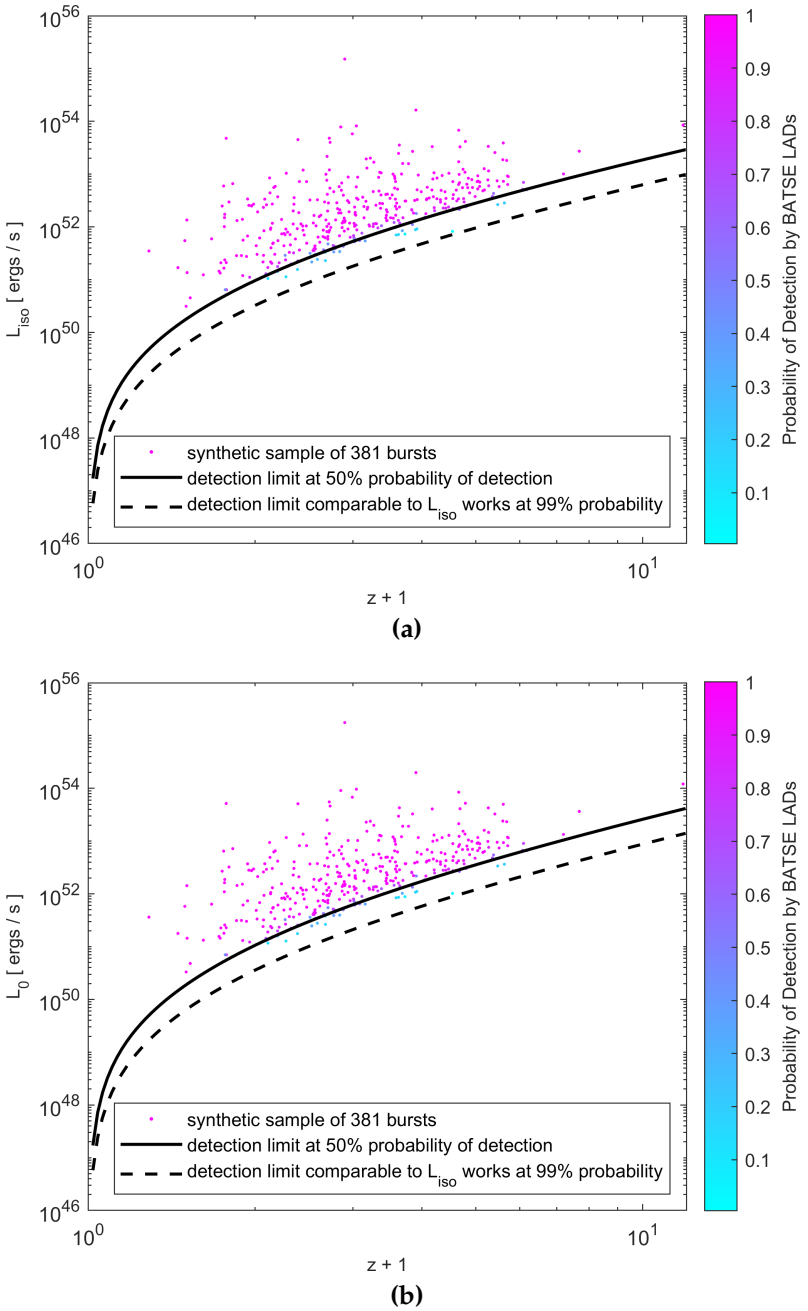

Figure 2.8: An illustration of the effects of detection threshold on the outcome of the Efron-Petrosian test statistic. Plot **(a)** Shows the synthetic data set used for our study of $(L_{iso}, 1+z)$ correlation. The solid black line represents the detector threshold at 50% while the dashed black line represents a detector threshold comparable to that of L19 at 99% probability of detection. The color bar represents the probability of detection by the BATSE LADs where cyan and magenta represent 0% and 100% chances of detection, respectively. Plot **(b)** shows the redshift-evolution corrected data set based off of the value of alpha calculated using the detector threshold at 50% probability of detection.

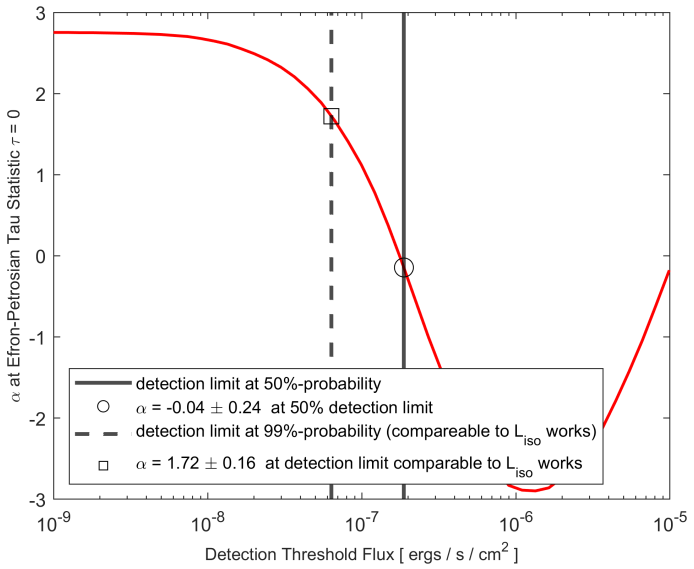

(c)

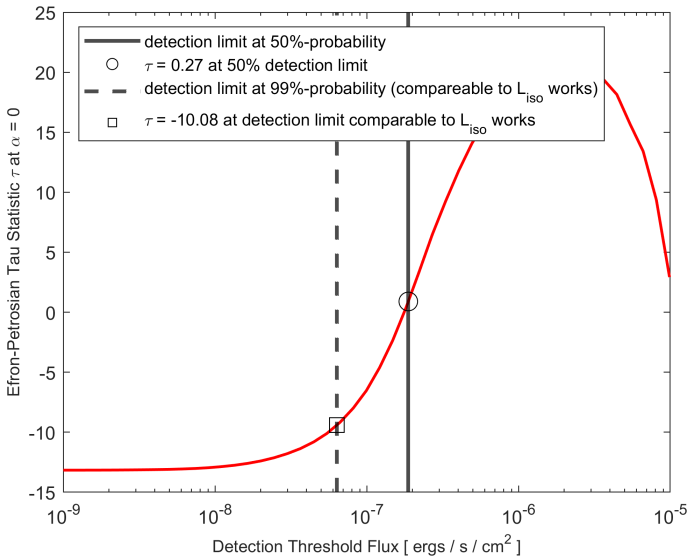

(d)

Figure 2.8: (cont.) Plot **(c)** shows the alpha value calculated corresponding to $\tau = 0$ with varying detection threshold limits. The solid black line represents the detector threshold at 50%, the black circle is the average α value over 50 generated samples for the specific threshold used, while the dashed black line represents the detector threshold at 99% probability of detection, comparable to those of previous studies, and the black square is the average α over 50 generated samples at $\tau = 0$. Plot **(d)** displays the τ statistic at $\alpha = 0$. The black line represents the detector threshold at 50% detection probability and the dashed black line represents the detection threshold at 99% detection probability, comparable to those of previous studies. The circle and square in this figure are the average τ values over 50 generated samples.

studies we used the method of Efron-Petrosian and the τ statistic to determine the exponent of the power-law relationship, α in $g(z) = (1+z)^{\alpha}$, between the luminosity/energetics and redshifts of LGRBs.

Contrary to the previous studies, we conclude that the effects of the detection threshold has been likely severely underestimated. We further confirm our conclusion via Monte Carlo simulation, where we assume no correlation between the energetics and the redshift of LGRBs. We then measure these simulated LGRBs via the BATSE detector (for its simplicity). Our finding is that **an underestimation of the effective detection threshold by even less than a factor of two can create artificial correlations between the redshifts and the luminosity/energetics of LGRBs**. The Monte Carlo simulation of P16 also shows that an underestimation of the detector flux limit can lead to apparent artificial correlations between luminosity and redshift. They further show that this effect can also give rise to an apparent overabundance of LGRBs at low redshift.

The regression slope (α, on a log-log plot) of the reported correlations between the redshift and the luminosity/energetics of previous studies also resembles their chosen detection threshold (Figures 2.1a, 2.3a, and 2.5a). This further corroborates our hypothesis that the observed correlations are an artifact of the individually chosen detection thresholds of the various gamma-ray detectors.

A more accurate study of the luminosity/energetics-redshift evolution requires a more careful modeling of the detection threshold of gamma-ray detectors, where the detection threshold is not a single cutoff on the distribution of LGRBs but rather a dispersed set of detection probabilities in the entire bivariate distribution. However, such a modeling approach is impossible with the original method of Efron-Petrosian and requires parametric modeling of the luminosity/energetics and redshift distribution as well as the detection threshold.

Le, Ratke, and Mehta (2020) uses purely parametric methods to determine the

GRB formation rate $\rho(z)$. They find that there is no deviation from the SFR at any redshift for the complete unbiased LGRB *Swift*-Perley and *Swift*-Ryan-b samples. They do, however, find an excess at low redshift $(z < 1)$ for the *Swift*-Ryan 2012 sample, and conclude that the reason for this excess is either incomplete sample size, that $\rho(z)$ doesn't trace SFR at low redshift, or that it is simply unclear.

Deng et al. (2016) run an in-depth analysis using both the τ statistic and parametric modeling and find that observational biases may lead to an overestimation of the α value, and that the evidence for luminosity evolution with redshift is too weak to argue. They note several biases that can lead to data sets being incomplete in redshift, such as the flux truncation effect, trigger probability, and redshift measurement. They too argue that the true instrument threshold for a GRB is complicated, as we have. Coward et al. (2013) goes into further detail on how the biases of redshift measurement are even more complicated, noting factors such as galactic dust extinction, redshift desert, and host galaxy extinction that contribute, independent of the brightness of a GRB. They argue that the observed redshift distribution is compatible with a GRB formation rate $\rho(z)$ that tracks the SFR.

The premise of the previous studies in §2.3 has been to provide a nonparametric investigation of the luminosity/energetics vs redshift. However, upon performing the nonparametric correlation, the majority of these investigations rely on parametric fitting of the luminosity/energetics and redshift distributions, which convolutes the premise. Indeed, Lan et al. (2019) presents a fully parametric study of the redshift/energetics evolution and reports a potential correlation between the two, but nevertheless, their study is founded on the assumption of a simple hard cutoff of the detection threshold of LGRBs. A fully parametric study of the correlation which incorporates a more accurate and detailed description of the detection threshold of gamma-ray detectors remains to be done.

2.6 Data Availability

All of the data used in this paper, as well as the Matlab code used for our analysis and Monte Carlo simulation, can be found here: https://github.com/cdslaborg/lgrbEnergeticsRedshiftCorrelation. The original data can also be found in the individual four papers analyzed in §2.3.

3 ALTERNATIVE STATISTICAL INTERPRETATION FOR THE APPARENT PLATEAUS IN THE DURATION DISTRIBUTIONS OF GAMMA-RAY BURSTS

Authors: Osborne, Joshua Alexander, Christopher Michael Bryant, Fatemeh Bagheri, and Amir Shahmoradi

Published: Astronomy & Astrophysics (A&A), 687 A122 (2024)

3.1 Introduction

Gamma-ray bursts (GRBs) are mainly split into two categories: long-duration GRBs (LGRBs), with $T_{90} > 2$ s, and short-duration GRBs (SGRBs), with $T_{90} < 2$ s (e.g., Kouveliotou et al., 1993). Specifically, T_{90} is the time it takes to receive 90% burst fluence, starting when 5% of the fluence has been observed (e.g., Poolakkil et al., 2021). Significant observational evidence over the past two decades has connected LGRBs to the death and the iron core-collapse of supermassive stars (Fruchter et al., 2006; Woosley and Bloom, 2006). Specifically, the leading theory points toward Wolf-Rayet stars, with masses between $10M_{\odot} - 50M_{\odot}$ (Massey, 1981), as being the most likely progenitors of LGRBs due to the mass loss incurred due to stellar wind, allowing for the jets to break out of the stellar envelope. This collapsar model of LGRBs was first supported by observational evidence through the association of half a dozen GRBs with spectroscopically confirmed broad-line Ic supernovae (SNe), as well as photometric evidence of underlying SNe in about two dozen more (Galama et al., 1998; Hjorth et al., 2011; Hjorth et al., 2003; Stanek et al., 2003; Woosley and Heger, 2006). In addition, there is indirect evidence for the connection of LGRBs with massive stars from the identification of LGRB host galaxies as intensively star-forming galaxies (Bloom et al., 2002; Christensen, Hjorth, and Gorosabel, 2004; Fruchter et al., 2006; Le Floc'h et al., 2003). The LGRBs are localized in the most active star-forming regions within those galaxies, increasing the probability that they originate from the death of supermassive stars. Physically, according to the Collapsar model, as the core collapses in a supernova (SN) explosion, a bipolar jet is launched from the center of the star that has to drill through the stellar envelope and break out to produce an observed GRB (e.g., MacFadyen and Woosley, 1999; MacFadyen, Woosley, and Heger, 2001).

While the evidence for a LGRB-supernovae association (Bloom, Frail, and Sari,

2001) has provided strong support for the collapsar model, the first strong sign of support for the jet-ejecta interaction has come from the off-axis afterglow observations of GRB 170817A (e.g., Abbott et al., 2017a; Goldstein et al., 2017; Savchenko et al., 2017a). In their study, Bromberg, Nakar, Piran, et al. (2012) developed a model of LGRBs that provides the first prompt-emission observational imprint of this jet-envelope interaction, and thus, direct confirmation of the collapsar model. A distinct signature in the duration distribution has been detected: the appearance of a plateau toward short durations. This occurs at times much shorter than the typical breakout time of the jet, that is, the time it takes for the jet to drill through the stellar envelope. This action dissipates energy, so the engine driving these jets must be in operation for at least the breakout time. If it is not, a GRB is not produced. The GRB is brief for breakout times that are very close to the engine time and a characteristic plateau is seen in the duration distribution. The breakout time is set by the density and radius of the stellar envelope at radii $> 10^{10}$ cm. In comparison, the stellar core properties at radii $< 10^{8}$ cm determine the engine's working time.

Unlike LGRBs, SGRBs are theorized to result from the merger of either two neutron stars (NS-NS) or that of a neutron star and a black hole (NS-BH) (Berger, 2014; D'Avanzo, 2015; Eichler et al., 1989; Metzger and Berger, 2012; Narayan, Piran, and Kumar, 2001). Recently, the first NS-NS merger was confirmed in an unprecedented joint gravitational and electromagnetic observation by Advanced Laser Interferometer Gravitational-Wave Observatory (LIGO), Advanced Virgo, INTErnational Gamma-Ray Astrophysics Laboratory (INTEGRAL) and the Fermi Gamma-ray Space Telescope's Gamma-ray Burst Monitor (GBM) (Abbott et al., 2017a; Goldstein et al., 2017; Savchenko et al., 2017b). Following the discovery of gravitational waves, this was also the first spectroscopically confirmed event associated with a kilonova. Other recent studies using photom-

etry have also found a kilonova event associated with GRB 211211A and GRB 230307A, both consisting of a hard-to-soft prompt emission (Levan et al., 2023; Troja et al., 2022). Compact binary mergers of these types are accompanied by significant dynamical mass ejection. Models differ with respect to how much mass is ejected depending on the GRB, from 0.03 - 0.08 $M_\odot$ (GRB 130603B) to 0.1 - 0.13 $M_\odot$ (GRB 060614) (Berger, Fong, and Chornock, 2013; Tanvir et al., 2013; Yang et al., 2015). The beamed nature of these events has been observed by inspecting breaks in optical and radio bands in GRB 990510 (Harrison et al., 1999). Similar observations of breaks in SGRB afterglows have suggested the involvement of jets as well (Fong et al., 2012; Soderberg et al., 2006). Further supporting evidence for relativistic jets in GRBs has been found thanks to the observation of superluminal motion in GRBs by Ghirlanda et al. (2019), Mooley et al. (2018), and Taylor et al. (2004), a phenomenon that is typically seen in the jets of blazars and quasars. Therefore, similarly to the collapsar model, the merger launches a relativistic jet that has to push through the expanding ejecta of significant mass (Duffell, Quataert, and MacFadyen, 2015; Gottlieb, Nakar, and Piran, 2018; Kumar and Zhang, 2015; Murguia-Berthier et al., 2014; Nagakura et al., 2014). According to Moharana and Piran (2017), this again produces a plateau in the T_{90} distribution, only at shorter durations than the one seen with LGRBs, reflecting the time it takes for prompt γ-ray emission to become observable after the jet reaches the ejecta's outer edge.

In this paper, we argue that although the plateaus seen in the analysis of the T_{90} distributions of GRBs by Bromberg, Nakar, Piran, et al. (2012) and Moharana and Piran (2017) could serve as a direct confirmation of theoretical models, they could (with equal plausibility) simply be interpreted as statistical artifacts. This work is organized as follows. Section 3.2 reviews and dissects the theoretical arguments for the collapsar interpretation of the observed plateau of LGRBs duration distri-

bution. Section 3.3 details our alternative statistical interpretation of the plateau and our attempt to reproduce the apparent plateaus seen in observational GRB durations from sample incompleteness. Section 3.4 presents a discussion of our results.

3.2 Collapsar interpretation of the plateau

The argument for the presence of a plateau in the observed duration distribution of LGRBs begins with the assumption that the intrinsic[1] prompt gamma-ray emission duration (t_γ) depends exclusively on the LGRB central engine activity time (t_e) and the jet breakout time (t_b) from the stellar envelope,

$$t_\gamma = \begin{cases} 0 & \text{if } t_e \leq t_b \,, \\ t_e - t_b & \text{if } t_e > t_b \,. \end{cases} \tag{3.1}$$

Realistically, as Bromberg, Nakar, Piran, et al. (2012) stated, the jet breakout, engine working times, and the gamma-ray emission duration might be correlated with each other and other properties of the LGRB progenitor. Nevertheless, assuming the validity of (3.1), we can write the probability density function (PDF) of t_γ (i.e., the probability distribution of the intrinsic LGRB duration) in terms of the PDF of the engine working time, t_e,

$$\pi_\gamma(t_\gamma)\mathrm{d}t_\gamma = \begin{cases} 0 & \text{if } t_e \leq t_b \,, \\ \pi_e(t_e)\mathrm{d}t_e = \pi_e(t_b + t_\gamma)\mathrm{d}t_\gamma & \text{if } t_e > t_b \,, \end{cases} \tag{3.2}$$

where π denotes the PDF. In other words, the duration distribution of LGRBs (for

[1]Note: Bromberg, Nakar, Piran, et al. (2012) use the keywords "intrinsic" and "observed" interchangeably to represent rest-frame LGRB duration. In this paper, "intrinsic" and "observed" exclusively refer to the GRB rest frame and the observer frame on Earth, respectively.

a given t_b) is simply the tail of the distribution of the engine work time beyond t_b. Under further assumption that π_e is locally analytic at $t_e = t_b$, the Taylor expansion of the right-hand side of (3.2) at $t_e = t_b$ yields,

$$\pi_e(t_b + t_\gamma) = \pi_e(t_b) + t_\gamma \frac{\mathrm{d}\pi_e(t_e)}{\mathrm{d}t_e}\bigg|_{t_e=t_b} + \mathcal{O}\left(t_\gamma^2\right) . \tag{3.3}$$

Given Eqs. (3.2) and (3.3), this implies a nearly constant PDF for the prompt emission duration of LGRBs as $t_\gamma \to 0$, that is, if and only if the higher order terms in the Taylor expansion are negligible compared to the first (constant) term. This requires either $t_\gamma \ll t_b$ or for all derivatives of $\pi_e(t_e)$ near t_b be nearly zero. Specifically, the second term in the right-hand side of Eq. (3.3) containing the first derivative of $\pi_e(t_e)$ must satisfy the following condition:

$$\frac{\mathrm{d}\pi_e(t_e)}{\mathrm{d}t_e}\bigg|_{t_e=t_b} \ll \frac{\pi_e(t_b)}{t_\gamma} . \tag{3.4}$$

Independent theoretical arguments (e.g., Bromberg, Nakar, and Piran, 2011) have suggested a typical jet breakout time $\hat{t}_b \simeq 50$ [s], which is on the same order as the starting point of the plateau behavior in the duration distribution of LGRBs at $\hat{t}_\gamma \simeq 20 - 30$ [s] (Bromberg, Nakar, Piran, et al., 2012). This similarity ($\hat{t}_\gamma \simeq \hat{t}_b$) clearly violates the condition of $t_\gamma \ll t_b$ under which the Taylor expansion is valid. Bromberg, Nakar, and Piran, 2011; Bromberg, Nakar, Piran, et al., 2012 reconciled this by further assuming $\pi_e(t_e)$ is a smooth function that "does not vary on short timescales in the vicinity of $\hat{t}_b$;" namely: the first and higher order derivatives in the Taylor expansion must be effectively zero relative to the first constant term in Eq. (3.3).

Such a strict additional constraint on the derivatives in the Taylor expansion in Eq. (3.3) leads to a circular logic whereby the collapsar interpretation of the observed nearly-flat plateau in t_γ requires the assumption of a nearly-flat plateau in

engine working time distribution around t_b. We recall that $\pi_\gamma(t_\gamma > 0) = \pi_e(t_e > t_b)$, by definition based on Eq. (3.2). In other words, the collapsar interpretation of the plateau requires the implicit assumption of the existence of the plateau.

The above circular logic can be resolved in several ways: 1) the theoretical predictions of the typical breakout time $\hat{t} \sim 50$ [s] are imprecise; 2) the distribution of the engine activity time $\pi_e(t_e)$ is indeed nearly flat around $\hat{t}_b$; or 3) the observed plateau in the duration distribution of LGRBs does not have a collapsar interpretation, but is due, rather, to the statistical nature of the distributions of strictly positive physical quantities combined with sample incompleteness, convolution effects, contamination with SGRBs, and visual effects.

In the following section, we argue the last resolution offers a plausible explanation for the apparent plateaus in the duration distributions of both LGRBs and SGRBs, without invoking any physical theories.

3.3 Statistical interpretation of the plateau

Statistical distributions with strictly positive support, for example, $\pi(t_\gamma), t_\gamma \in (0, +\infty)$, frequently and naturally exhibit plateaus in their short tails. Such plateaus can appear across a broad range of independent circumstances, as discussed in the following subsections.

3.3.1 All finite-valued statistical distributions with positive support exhibit plateaus

We recall that the Taylor expansion of the PDF of an analytic statistical distribution at any point within its support guarantees the existence of a plateau near the point of expansion. Such a plateau, however, is mathematically infinitesimal, defined only asymptotically as one approaches the point of expansion. There-

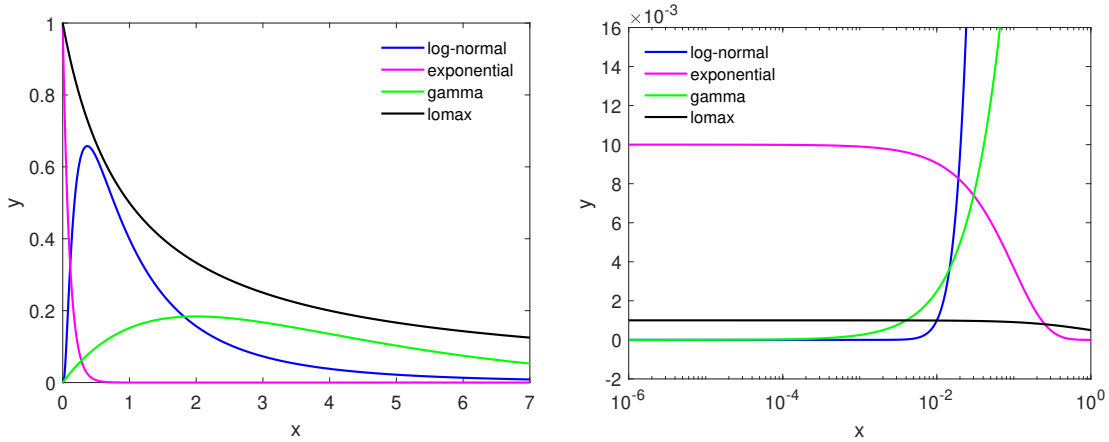

Figure 3.1: Illustration of the plateau in the distribution of strictly positive random variables as $x \to 0$. The existence of these plateaus is mathematically guaranteed for all distributions with positive support and finite-valued Probability Density Function (PDF). **(a)** PDFs of three popular positive-valued statistical distributions. **(b)** Zoom-in on the same PDFs as in plot (a), but at very small values near the origin, on a logarithmic x-axis, illustrating the plateau-like behavior of the distributions near $x = 0$. The appearance of the plateau near the origin ($x = 0$) is guaranteed by the logarithmic transformation of the x-axis. The logarithmic transformation effectively spreads a finite amount of variations in the PDF on the y-axis over a semi-infinite range on the (logarithmic) x-axis.

fore, these mathematically infinitesimal plateaus are invisible to the human eye almost anywhere within the support of the PDF, except at the origin, $t_\gamma = 0$, under an appropriate transformation. By definition, the PDF has a positive support $t_\gamma \in (0, +\infty)$. Therefore, taking the logarithm of the x-axis (t_γ) pushes the lower limit of the support of the PDF at $t_\gamma = 0$ to negative infinity: $\log(t_\gamma \to 0) \to -\infty$. This logarithmic transformation of the x-axis effectively infinitely magnifies the Taylor expansion of $\pi(t_\gamma)$ around $t_\gamma = 0$. This infinite magnification can be intuitively understood by noting that the PDF $\pi(t_\gamma)$ of the distribution must have a finite value at the origin, $t_\gamma = 0$, with a well defined, finite, right-hand derivative. When the x-axis is logarithmically transformed, the finite amount of changes in $\pi(t_\gamma)$ span progressively over larger and larger logarithmic ranges on the x-axis, effectively making the PDF resemble a plateau as $\log(t_\gamma) \to -\infty$.

This is precisely the mechanism by which the collapsar interpretation discussed in Sect. 3.2 attempts to explain the observed plateau in the duration distribution of LGRBs. However, the collapsar theory of LGRBs invocation appears unnecessary since all finite-valued statistical distributions with strictly positive support exhibit a plateau toward zero, and there is an uncountably infinite number of such statistical distributions. Given that the gamma-ray duration, t_γ, of both SGRBs and LGRBs is a strictly positive-valued observable random variable, the appearance of a plateau in their t_γ distributions on a $\log(t_\gamma)$-axis is mathematically guaranteed as $t_\gamma \to 0$. This is true without recourse to any physical theories of GRBs. Figure 3.1 illustrates this mathematical asymptotic plateau behavior for some well-known continuous distributions with positive real support.

3.3.2 Sample-incompleteness creates plateaus in observational data

Despite the mathematical guarantee of a plateau in strictly positive finite-valued distributions, the practical visibility of such plateaus in observational data is limited to distributions whose probability mass is heavily concentrated around zero. For an illustration, the near-zero, hard-to-sample, mathematical plateaus of gamma and lognormal distributions from this category are depicted in Figure 3.1b.

Sample-incompleteness, however, can still generate a second kind of plateau in strictly positive statistical distributions, entirely different from the plateaus of the first kind of mathematical origin discussed in Sect 3.3.1. Such observational plateaus result from limited sampling of positive statistical distributions that are highly positively skewed. We recall that plateaus naturally also occur in the neighborhood of the mode of a distribution where the derivative of the PDF is mathematically zero. This flatness of the PDF around the mode can readily become observationally visible if the distribution sharply rises from some finite value at $t_\gamma = 0$, typically $\pi(t_\gamma = 0) = 0$, to the PDF mode at $t_\gamma = \hat{t}$, and gradually declines to zero as $t_\gamma \to +\infty$. This sharp rise and gradual decay is the typical behavior of many positive-valued statistical distributions and the key requirement for generating finite-sample extended plateaus in their PDFs.

Therefore, if the shape of the distribution (in log-log space) is such that the probability of sampling at $t_\gamma < \hat{t}$ is negligible, a plateau appears in the histogram of observational data at $t_\gamma \sim \hat{t}$. The plateau appearance is substantially strengthened and extended if the PDF decays slowly (and concavely) toward $+\infty$ and the observational sample is binned and visualized on a logarithmic x-axis as done in Bromberg, Nakar, Piran, et al. (2012).

To illustrate this artificial finite-sample plateau creation in action, we consid-

ered the lognormal distribution, widely used in astronomy for modeling luminosity functions and other observational data (e.g., Balazs et al., 2003; Berkhuijsen and Fletcher, 2012; Butler, Bloom, and Poznanski, 2010; Medvedev et al., 2017; Osborne, Shahmoradi, and Nemiroff, 2020; Shahmoradi, 2013a,b; Shahmoradi, 2017; Shahmoradi and Nemiroff, 2015; Yan et al., 2021; Zaninetti, 2018). The lognormal distribution is always positively skewed for any parameter values. This results in a typically negligible area to the left of the PDF mode, as illustrated in Figures 3.2a and 3.2c. Hence, the short tail of the lognormal distribution to the left of its mode is rarely fully observationally constructed, leading to the appearance of a plateau in the PDF on the log scale near the distribution mode. This behavior is not exclusive to lognormal and is generically seen in many statistical distributions with positive support, some of which are also shown in the rest of the plots of Figure 3.2.

3.3.3 Convolution creates plateaus in observational data

In addition to the area to the left of the mode of PDFs with positive support, the smoothness (differentiability) and concavity of the PDF near its mode play a dominant role in the appearance of finite-sample plateaus. Indeed, a separate class of statistical distributions with strictly positive support has modes that are neither smooth nor occur at the origin. These distributions, as shown by the Pareto and log-Laplace examples, hardly exhibit plateau behavior under finite sampling. Nevertheless, this section shows that even the most difficult, non-analytic, non-smooth PDFs can exhibit plateaus under convolution.

Recall the convolution of two functions:

$$(f * g)(t) = \int_{-\infty}^{\infty} f(\tau) g(t - \tau)\, d\tau\,, \tag{3.5}$$

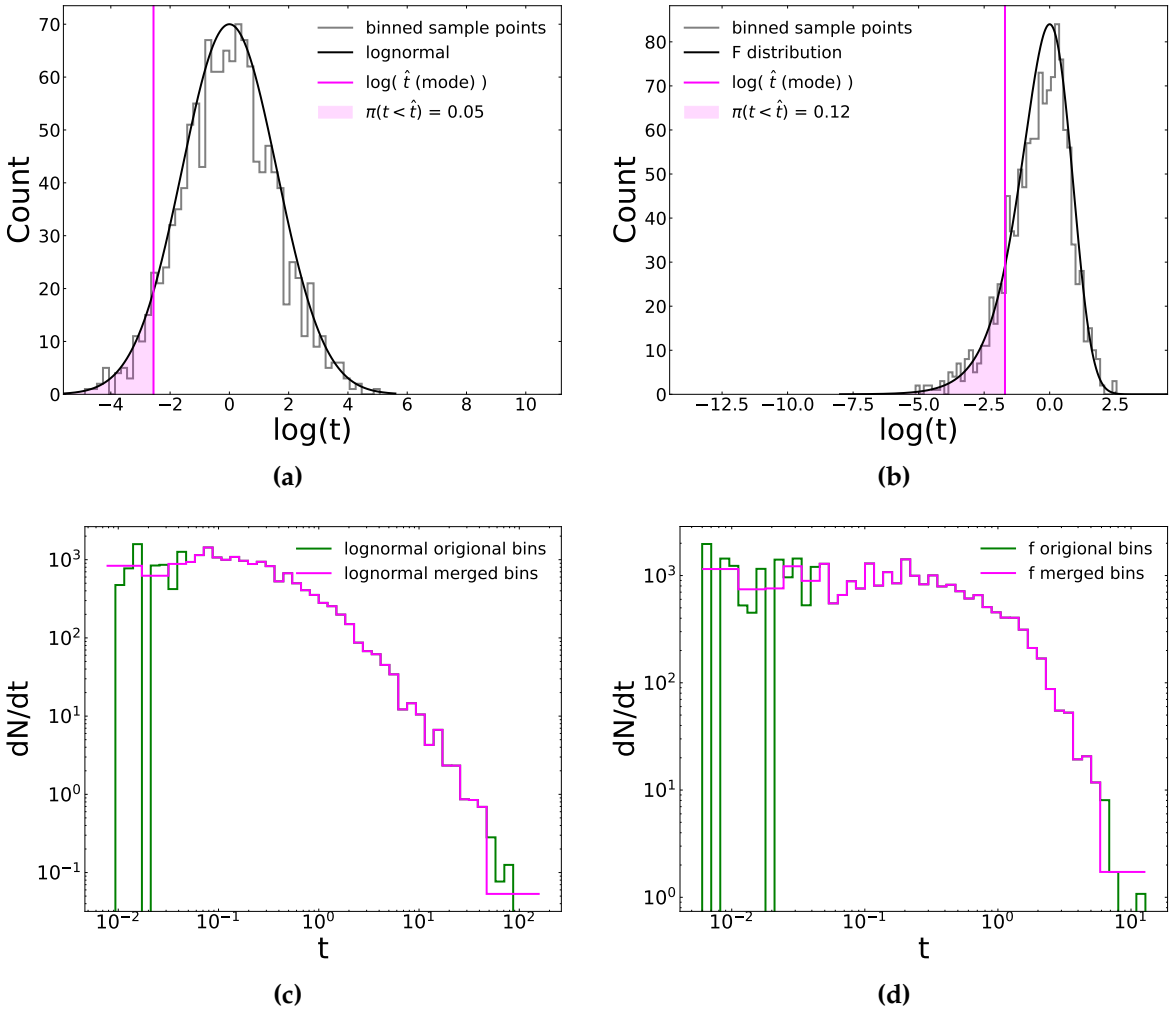

Figure 3.2: Illustration of the effects of sample incompleteness on plateau formation in statistical distributions. A primary factor in the appearance of finite-sample plateaus near the modes of PDFs is the area to the left of the PDF mode. The smaller this area, the fewer opportunities there are to construct the short tail of the PDFs in finite sampling, thus leading to the appearance of plateaus in the PDFs near their modes. Plots **(a)** & **(b)** depict the histograms of the log-transformed random variables drawn from select statistical distributions with positive support. Plots **(c)** & **(d)** depict the corresponding histograms of the original random variables but on logarithmic axes.

acts as a smoothing operation similar to that of weighted averaging. The resulting function from the convolution will be at least as smooth as the individual functions ($f(\cdot)$ or $g(\cdot)$ in (3.5)). In fact, the convolution operation is identical to a weighted dynamic averaging of $f(\cdot)$ when the weight, $g(\cdot)$, is a probability density function. In the case of the duration distribution of LGRBs, the convolution performed to obtain the observer-frame duration distribution is as follows:

$$\log(t_{\gamma,obs}) = \log(z+1) + \log(t_{\gamma,int}) \,, \tag{3.6}$$

where “obs" and “int" stand for the observed and intrinsic durations, respectively, and z represents the GRB redshift.

We demonstrate the effectiveness of convolution in creating plateaus by considering a Pareto PDF for the duration distribution of LGRBs. The Pareto distribution does not exhibit any plateau-like behavior within its support under any circumstances (e.g., see Figure 3.3a). Yet, when convolved with the redshift distribution of LGRBs detected by the Neil Gehrels Swift Observatory[2], the sharp non-analytical mode of the Pareto PDF transforms into a continuous smooth mode as seen in Figure 3.3b. Combining the observed convolved duration distribution of LGRBs with the duration distribution of SGRBs further eliminates the appearance of any discontinuity or sharp decline in the short tail of the distribution, leading to a plateau in the mixture distribution that is even longer than the observed plateaus in the duration distributions of The Burst And Transient Source Experiment (BATSE) and Fermi catalog GRBs (Figure 3.3c).

To verify the generality of convolution effects on plateau creation, we also considered four additional popular GRB formation rate scenarios, each in 10,000 independent simulations: Collaboration et al. (2018) (F18), Madau and Fragos (2017) (M17), Butler, Bloom, and Poznanski (2010) (B10), and Hopkins and Bea-

[2] All redshifts are taken from the Swift GRB catalog.

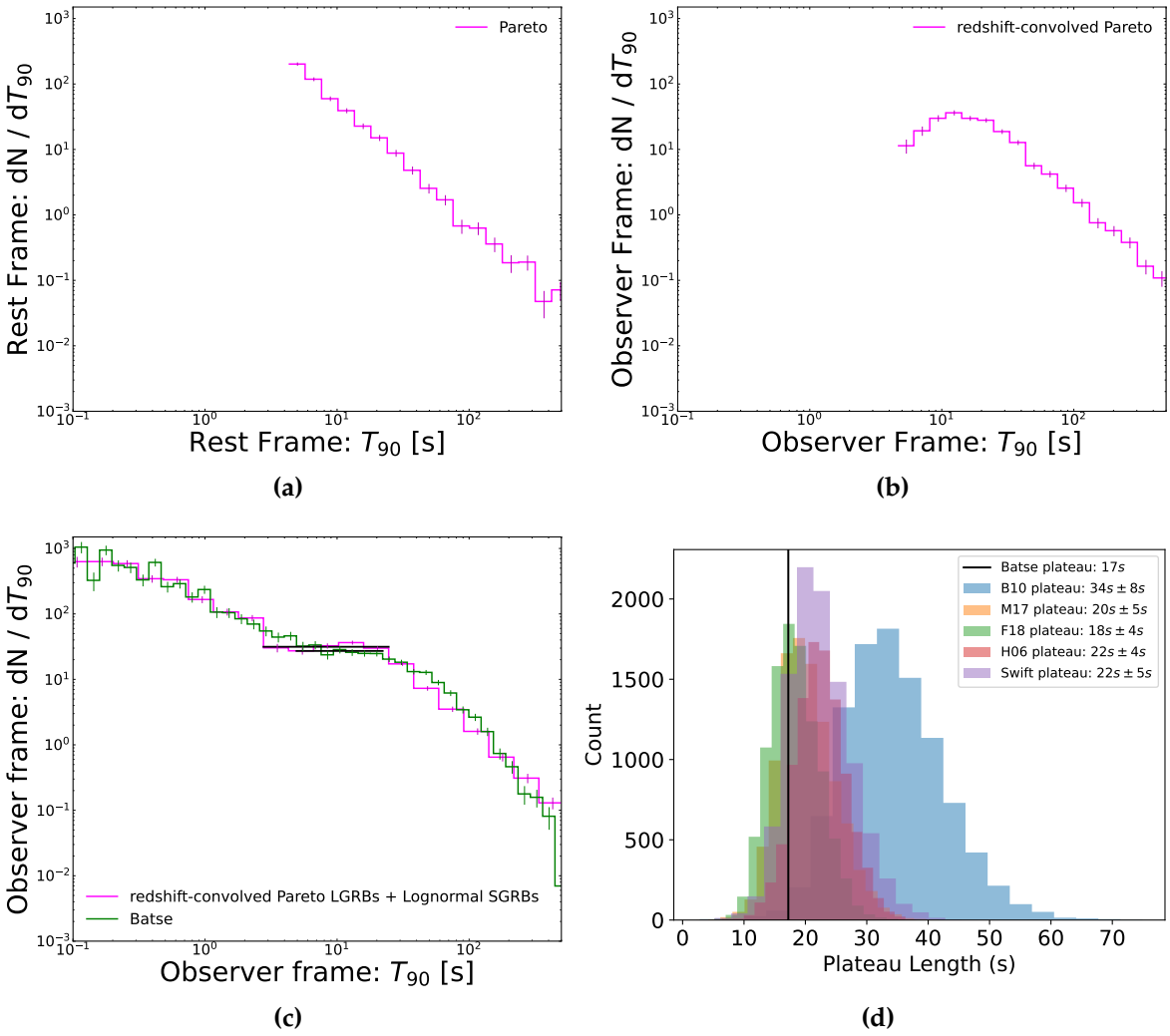

Figure 3.3: Illustration of the smoothing effects of convolution on the Pareto distribution, leading to the appearance of a plateau in $\frac{dN}{dT}$ plot. **(a)** Sampled points from a Pareto distribution after performing the bin merging as described in Bromberg, Nakar, Piran, et al. (2012). **(b)** Same data as in plot (a) but convolved with the redshift distribution of LGRBs (derived from Swift catalog). **(c)** Convolved observed duration distribution of LGRBs combined with a lognormal fit to the redshift distribution of SGRBs. For comparison, the green line represents the duration distribution of the BATSE SGRBs and LGRBs. The final observed plateau resulting from the Pareto distribution is 50% longer than the observed plateau in the duration distribution of BATSE LGRBs. **(d)** Distribution of the average plateau lengths, assuming an intrinsic Pareto duration distribution convolved with various GRB popular redshift distribution scenarios from the literature as listed in the plot legend. The observed plateau length in the BATSE duration data is illustrated by the vertical black line.

com (2006) (H06). The data modeling and fittings were performed by assuming one of these redshift models as the redshift distribution of LGRBs and assuming a parametric form for the intrinsic duration distribution of LGRBs (e.g., Pareto), using a Bayesian fitting approach, as described in Osborne, Shahmoradi, and Nemiroff (2020), Shahmoradi (2013a), Shahmoradi (2017), and Shahmoradi and Nemiroff (2015) assuming non-informative objective priors for all unknown parameters. Once the model fitting was carried out, random redshift samples of the same size as the observational duration distribution data were generated by sampling the corresponding redshift distribution models with an adaptive Markov chain Monte Carlo algorithm (Kumbhare and Shahmoradi, 2020; Shahmoradi and Bagheri, 2020a,b; Shahmoradi and Bagheri, 2021; Shahmoradi, Bagheri, and Osborne, 2020). The random samples were subsequently convolved with the random samples from the corresponding duration distribution models with the best-fit parameters to generate the observed duration distributions. This procedure was repeated 10,000 times for each modeling and redshift distribution scenario. Finally, the lengths of the resulting apparent plateaus in the duration distributions for each of the 10,000 simulations per modeling scenario were measured using the same approach as in Bromberg, Nakar, Piran, et al. (2012).

The histograms of the resulting plateau lengths for each of the five redshift distribution scenarios are illustrated in plot (d) of Figure 3.3d. Notably, the resulting average plateau lengths from the convolution of a Pareto duration distribution with all GRB formation rate scenarios are longer than the plateau length in BATSE observational data.

3.3.4 Sample contamination creates plateaus in observational data

A contamination of the short tail of the duration distribution of LGRBs with SGRBs leads to a further extension of the apparent plateaus because the population of SGRBs compensates for any drop in the count of LGRBs toward low durations. Again, we considered a lognormal fit for the intrinsic duration distribution of LGRBs. Osborne, Shahmoradi, and Nemiroff (2020), Shahmoradi (2013a,b), and Shahmoradi and Nemiroff (2015) argued and provided evidence for the goodness of fit of LGRBs and SGRBs prompt duration distributions with lognormal PDF. The lognormal distribution does not exhibit an inherent plateau near its short tail. Sample incompleteness, however, creates the appearance of a plateau in the lognormal fit to the observational LGRB data. This apparent plateau is further extended by the convolution of the intrinsic duration distribution with redshift to obtain the observe-frame duration distribution as illustrated in Figure 3.4a. Finally, the contamination with SGRB data due to the overlap of the two distributions completely eradicates any signs of decline in the short tail of LGRBs duration distribution, yielding a perfect plateau appearance in the final mixture distribution, as shown by the magenta solid curve in Figure 3.4a.

3.4 Discussion

In this paper, we present statistical arguments that strongly favor a non-physical (i.e., non-collapsar) origin for the observed plateau in the duration distribution of LGRBs. The Taylor expansion in Eq. (3.3) of the density function of the engine activity time (t_e) near the jet breakout time (t_b) requires the plateau to appear at durations orders of magnitude smaller than the inferred t_b in Bromberg, Nakar, Piran, et al. (2012). Bromberg, Nakar, and Piran, 2011; Bromberg, Nakar, Piran, et

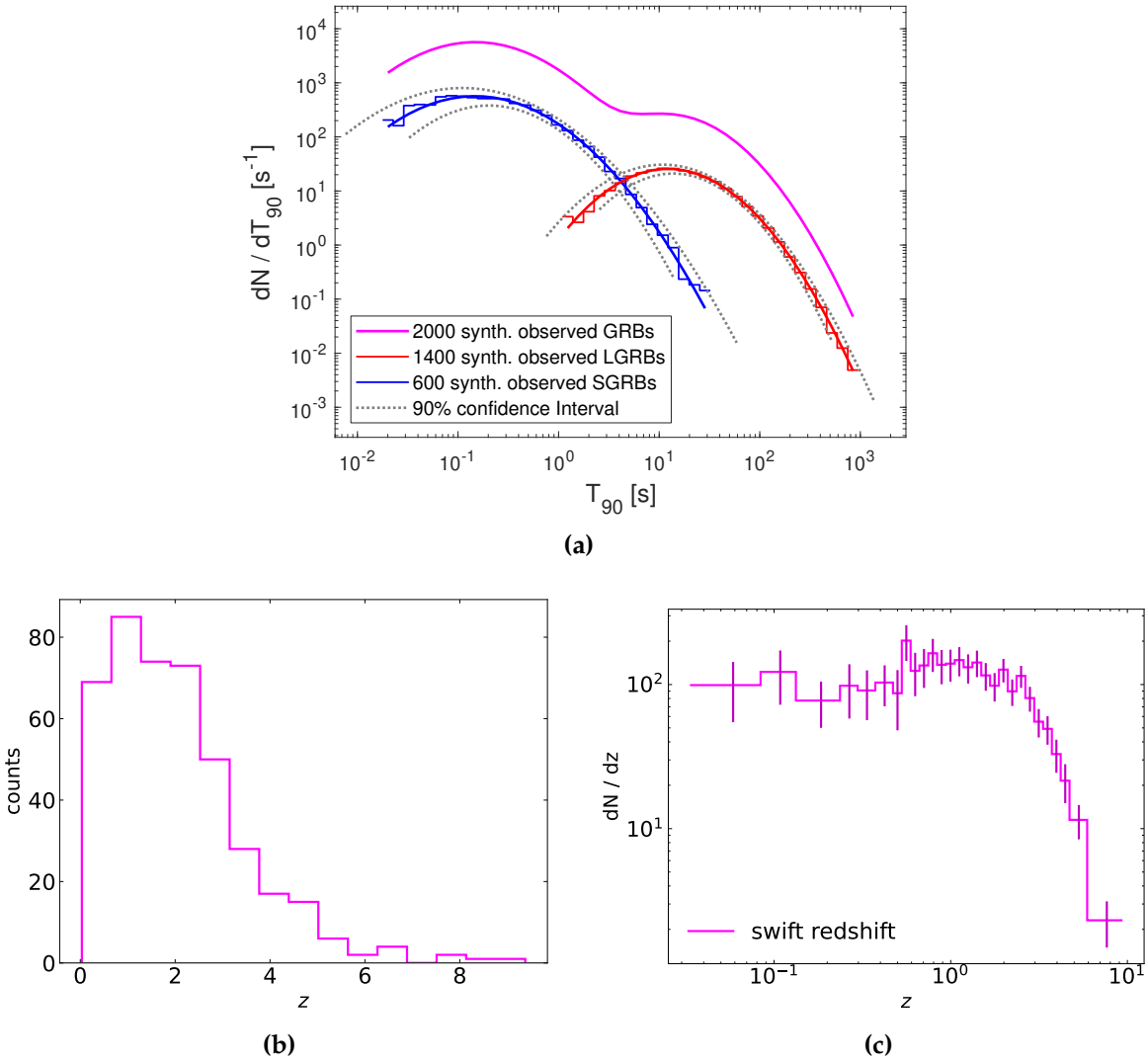

Figure 3.4: BATSE-detectable samples of 600 SGRBs and 1400 LGRBs are randomly generated from our respective Monte Carlo Universes. **(a)** SGRBs, represented by the blue bins and LGRBs by the red bins, where each bin is the 50th percentile value of 10,000 synthetic detections. The solid blue and red lines are lognormal fits to the bins in the pre-transformed space. These two fits are summed to produce the solid magenta line multiplied by a factor of 10 to offset it for clarity. The dotted gray lines represent the 90% confidence interval for each binned distribution. **(b)** Distribution of observed Swift redshifts in linear space. **(c)** Redshift distribution transformed in the same manner as the duration distribution throughout this manuscript. After performing the transformation described in Bromberg, Nakar, Piran, et al. (2012), the resulting plot displays a plateau in the log-log space, although there is no apparent physical origin.

al., 2012 reconciled this inconsistency by an additional assumption of the engine activity time as "a smooth function" that not vary on short timescales near the breakout time. However, this leads to a circular logic in the argument for the collapsar origin of the observed plateau, where Bromberg, Nakar, Piran, et al., 2012 imposed a flatness condition on the distribution of the engine activity time near the breakout time to obtain a flatness in the prompt duration of LGRBs; by definition as per Eq. (3.2), this is the same as the engine activity time at $t_\gamma > t_b$. Alternatively, we can interpret the plateau in the duration distribution of LGRBs as a constraint on the shape of the engine activity time, under the assumption that the prompt gamma-emission duration precisely reflects the engine activity time at $t_\gamma > t_b$, as proposed in Bromberg, Nakar, and Piran, 2011; Bromberg, Nakar, Piran, et al., 2012. In either case, the plateau in the duration distribution of LGRBs does not appear to serve as an observational imprint of the collapsar model.

We further question any physical origins of the observed plateau by showing that plateaus are ubiquitous in the short tails of statistical distributions with strictly positive support (e.g., Figure 3.2) and frequently result from a combination of sample incompleteness with the extremely positively skewed nature of such distributions (on natural axes). Even where the intrinsic duration distribution of LGRBs does not exhibit a plateau behavior in its short tail, we show that its convolution with a redshift distribution can create observed duration distributions that exhibit plateau-like behavior. The presence and extent of the plateaus are further significantly enhanced if SGRBs mix with and contaminate the observed duration distribution of LGRBs, as is the case with all major GRB catalogs. An example of a perfect plateau resulting from such contamination is depicted in Figure 3.4a.

To resolve the sample contamination problem and minimize the impact of SGRBs

duration distribution on the observed plateau in the duration distribution of LGRBs, Bromberg, Nakar, Piran, et al. (2012) also restricted their analysis only to soft LGRBs in the BATSE catalog. This is done by removing any events with a hardness ratio [3] above 2.6. This artificial cutoff preferentially excludes SGRBs from the duration histogram and significantly extends the observed plateau of LGRBs to more than twice the original length. However, in contrast to the arguments of Bromberg, Nakar, Piran, et al. (2012), this plateau extension in the population of soft LGRBs has no connection with the collapsar interpretation of the plateau. It is merely an artifact of further censorships and sample incompleteness caused by the exclusion of an arbitrarily chosen subset of data. To illustrate this phenomenon, we followed Osborne, Shahmoradi, and Nemiroff, 2020; Shahmoradi, 2013a; Shahmoradi and Nemiroff, 2015 to fit the BATSE catalog data with a comprehensive model for the duration, spectral peak energy, peak luminosity, and isotropic energy of GRBs. Notably, we assumed that the duration distributions of both LGRBs and SGRBs follow lognormal, making no assumption on the existence of plateaus in the duration distributions. Once the fitting was performed, we followed the prescription of Bromberg, Nakar, Piran, et al. (2012) to remove the observed events from our Monte Carlo Universe with hardness ratios larger than 2.6. Figure 3.5 compares the resulting duration histogram for the soft population of LGRBs with the original histogram from the Monte Carlo Universe. A few remarks are in order, as follows.

Firstly, plateaus appear in the duration distributions of both LGRBs and SGRBs without even requiring their existence in the model. Secondly, the LGRB plateau extends to about two orders of magnitude when we follow the prescription of Bromberg, Nakar, Piran, et al. (2012) to exclude short hard bursts from the histogram. While it is indeed purely statistical, this plateau extension is on par with

[3] The hardness ratio is defined as the ratio of fluence between BATSE energy channels. In this case, channels 3 (100-300 keV) and 2 (50-100 keV)

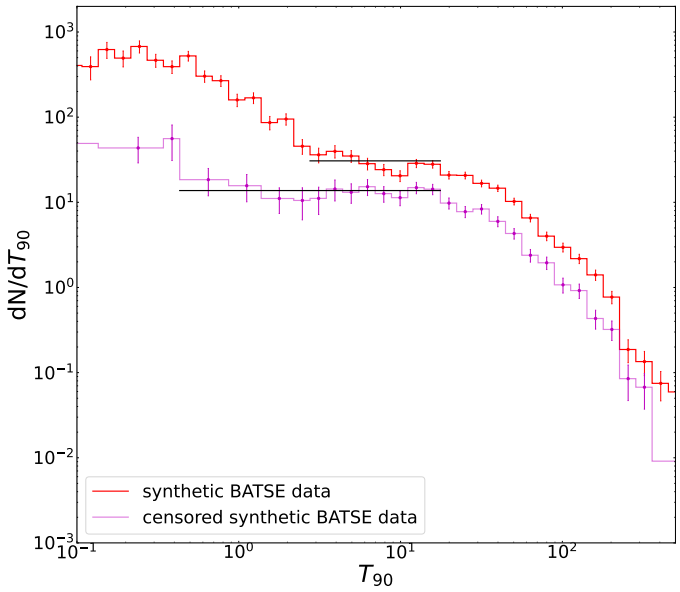

Figure 3.5: Illustration of the impact of excluding SGRBs from the duration distribution on the observed plateau of LGRBs. The original plateau in the red histogram and the extension of it by removing SGRBs in the magenta histogram are purely statistical (resulting from the log-normal fits to data as depicted in Figure 3.4a) and have no connections to the physics of GRBs or collapsars whatsoever.

the reported extension Bromberg, Nakar, Piran, et al. (2012) found in the BATSE catalog data.

The specific binning approach used to construct histograms of data also appears to moderately (and even significantly) impact the strength and extent of any plateau in the short tails of distributions. This binning effect is well illustrated in Figures 3.2c and 3.2d. The above arguments point to a non-physical origin for the observed plateau in the duration distribution of LGRBs. In fact, the distributions of other observational properties of GRBs (e.g., the observed redshift distribution as seen in Figure 3.4c) also exhibit plateaus without any apparent physical origins.

The plateau emerging within the LGRB duration distribution is not unique and can also be seen in the population of SGRBs. Unlike the population of LGRBs, the decline in the short tail of the duration distribution of SGRBs is readily seen. This

decline in the short tail actually suggests the reason why we do not see such a fall in the short tails of LGRBs duration distribution. Unlike the case of LGRBs, no additional mixing distribution "covers" this decline in the SGRB population. Such a plateau in the SGRB duration distribution is hard to reconcile with the non-collapsar origin of SGRBs. Moharana and Piran (2017) proposed a similar prompt emission mechanism to that of LGRBs (by requiring the SGRB jet to drill through an envelope) to explain the non-collapsar plateau seen in the duration distribution of SGRBs. The likelihood ratio test used in Moharana and Piran (2017) for comparing the performances of the lognormal and plateau models to observational data only applies to nested statistical models, while the models compared are non-nested with entirely different parameters. To compare the goodness of fit of different models to the combined SGRB and LGRB BATSE data, we also considered four modeling scenarios: the lognormal+lognormal mixture model as illustrated in Figure 3.4; the proposed plateau+powerlaw-plateau+powerlaw(tapered) mixture model as in Eq. (3) in Moharana and Piran (2017); lognormal - plateau + powerlaw (tapered) mixture model; and plateau+powerlaw-lognormal mixture model. The resulting fits yield the corresponding Bayesian information criterion (BIC) scores of: 8339, 8354, 8360, and 8362, implying that the observational SGRB/LGRB data is $\sim 3 \times 10^6 - 10^9$ times more likely to have originated from a lognormal+lognormal mixture model than any alternative models with plateaus for the duration distributions of either or both GRB classes.

By contrast, the statistical arguments presented in this manuscript offer a natural explanation for plateaus in the duration distributions of both GRB populations without recourse to any physical arguments and origins of GRBs. The fact that a wide variety of statistical distributions fit the duration distributions of GRBs equally well, as we demonstrate in this work, further corroborates the findings of Ghirlanda et al., 2015; Salafia et al., 2020 and serves as a reminder to exercise

caution in attributing the observed plateaus in the duration distributions of GRBs to their physics.

In summary, we present an alternative equally plausible purely statistical origin for the observed plateaus in the duration distributions of LGRBs and SGRBs. Our analysis further signifies the relevance and importance of selection effects and data censorship (e.g., Band and Preece, 2005; Bryant, Osborne, and Shahmoradi, 2021; Butler, Bloom, and Poznanski, 2010; Butler, Kocevski, and Bloom, 2009; Butler et al., 2007; Coward et al., 2015; Hakkila et al., 2003; Lloyd and Petrosian, 1999; Lloyd, Petrosian, and Mallozzi, 2000; Nakar and Piran, 2004; Osborne, Bagheri, and Shahmoradi, 2021; Osborne, Shahmoradi, and Nemiroff, 2020; Petrosian, Kitanidis, and Kocevski, 2015; Petrosian and Lee, 1996; Petrosian, Lloyd-Ronning, and Lee, 1999; Shahmoradi, 2013b; Shahmoradi and Nemiroff, 2011a; Shahmoradi and Nemiroff, 2009; Shahmoradi and Nemiroff, 2011b; Tarnopolski, 2021) in data-driven studies of the Physics of GRBs.

4 Discussion

4.1 Overview

The overarching purpose of this thesis is to enhance the reliability of GRB studies by identifying and addressing the roles of bias and sample incompleteness. By doing so, this research aims to provide a more accurate understanding of GRBs and improve the methodologies used in their analysis. In this chapter, I will summarize the main results of the research projects presented in this thesis, expanding on a few points, followed by concluding remarks.

4.2 Summary of Findings

In Chapter 2, a reanalysis of the works of Y15, P15, P16, T17, and L19 found that the effects of the detector threshold were likely underestimated in each study, giving rise to apparent artificial correlations between luminosity and redshift. This in turn led to an apparent overabundance of LGRBs at low redshift and gave rise to the problem of the GRB formation rate deviating from the SFR. This hypothesis was further tested by creating a synthetic dataset of LGRBs generated with no correlation between their energetics and redshifts. The dataset was subjected to censorship as would occur with a real-world detector, and the correlation be-

tween energetics and redshift was again computed as before. It was found that an underestimation of the effective detector threshold yielded an artificial correlation that was not a part of the original generated data. Furthermore, this gave rise to an overabundance of LGRBs at low redshift that was also not the case in the synthetic dataset.

Following this in Chapter 3, the evidence for the collapsar origins of LGRBs in T_{90} duration distributions was reexamined and found to more likely be the result of statistical methods rather than the physics of the progenitor. Multiple statistical artifacts were shown to potentially contribute to the apparent plateau that has been interpreted as validation of the collapsar model. When viewed on a logarithmic scale, all finite-valued statistical distributions with positive support will develop a plateau as the axis is stretched on approach to zero. Sample contamination between the SGRB and LGRB subsets produce an interior plateau as the tails between their respective modes overlap.

Of particular note is sample incompleteness, as it is one of the more pervasive statistical challenges in data analysis. I will briefly expand on an example from Section 3.3.2. Figure 4.1 more clearly demonstrates the effect of sample incompleteness relative to a more complete sample of the lognormal distribution, specifically. The left column is a random sampling of a lognormal distribution with 100,000 samples drawn. The right column is similar, but with only 600 samples drawn. The data is transformed in the bottom row from Counts $\rightarrow dN/dt$ by dividing each bin by its width. Since the binning is done in log-space the width of each bin varies, growing larger as t grows. The left tail of the distribution is elevated because each bin is being divided by progressively smaller numbers as you move leftwards. The effect on the incomplete sample is more extreme, however, and it begins to flatten out. Merging adjacent bins that have less than five events

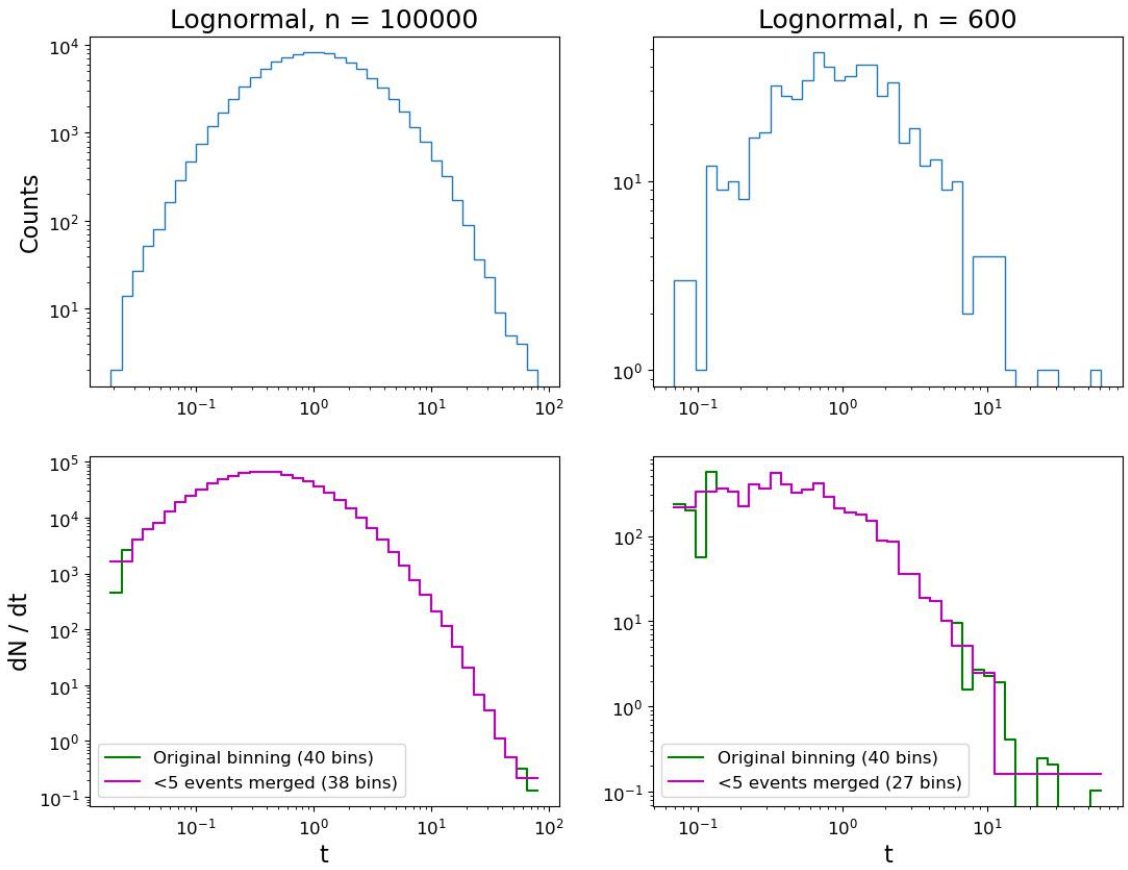

Figure 4.1: The effect of sample incompleteness on the transformed data of a lognormal distribution. There is an apparent plateau to the left of the mode of the incomplete sample (bottom right figure).

each also contributes to this effect. This highlights how the interplay between sample incompleteness and the way in which the data is commonly transformed and visualized for GRB T_{90} duration datasets leads to the artificial appearance of a plateau without it existing in the underlying distribution.

Using the BIC to Evaluate Models

In Section 3.4, it is briefly mentioned that the Bayesian information criterion (BIC) was used to determine that a lognormal-lognormal mixture is the most likely underlying distribution of observed BATSE SGRB/LGRB duration data. I will expand on that here. First and foremost, BIC is a statistical measure used for model selection among a finite set of models (Schwarz et al., 1978). It helps identify the model that best balances goodness of fit and model complexity by penalizing an excessive use of parameters, thus preventing overfitting. It can be used to compare non-nested models, where one model is not a special case of another model. This is unlike the likelihood ratio test, which is only appropriate for comparing nested models.

The BIC is defined as

$$\mathrm{BIC} = k \ln n - 2 \ln \hat{L} \tag{4.1}$$

where

$$\hat{L} = p\left(x \mid \hat{\theta}, M\right)$$

Here, $\hat{L}$ is the maximized value of the likelihood function of model M. x is the observed data and n is the number of data points in it. $\hat{\theta}$ are the parameter values that maximize the likelihood function, and k is the number of parameters of model M. When comparing the BIC of two models, the one that yields the lowest

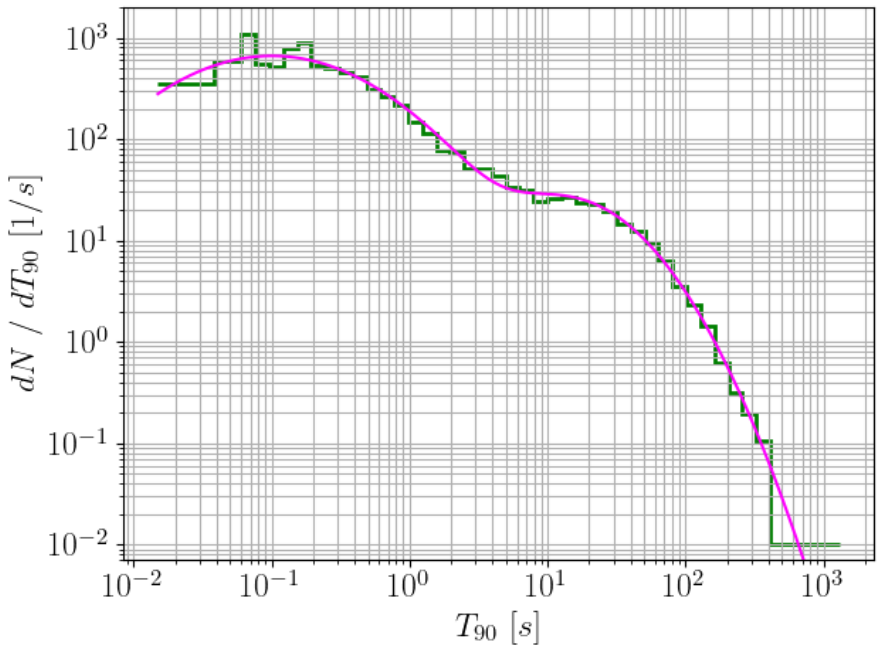

Figure 4.2: Comparing the fit of the best lognormal-lognormal mixture model (pink) to the BATSE dataset (green) of T_{90} values. The BIC for this model is 8339, the lowest (i.e., best fit) of the four models.

value is the most desirable. This can be explicitly quantified by approximating the Bayes Factor (BF) to find the posterior probability of models. In terms of BIC values,

$$\mathrm{BF}_{12} \approx \exp\left(\frac{\mathrm{BIC}_2 - \mathrm{BIC}_1}{2}\right) \tag{4.2}$$

and it indicates how many times more likely the observed data x was drawn from model M_1 than M_2 (Wagenmakers, 2007).

Returning to the discussion on whether or not the apparent plateau in the observed T_{90} BATSE duration data is intrinsic to the underlying distribution, or a statistical artifact, BIC was used to compare and quantify the goodness of fit of several models. Four models were considered: a lognormal & lognormal mixture model; a plateau plus powerlaw & plateau plus powerlaw (tapered) mixture model; a lognormal & plateau plus powerlaw (tapered) mixture model; and finally a plateau plus powerlaw & lognormal mixture model.

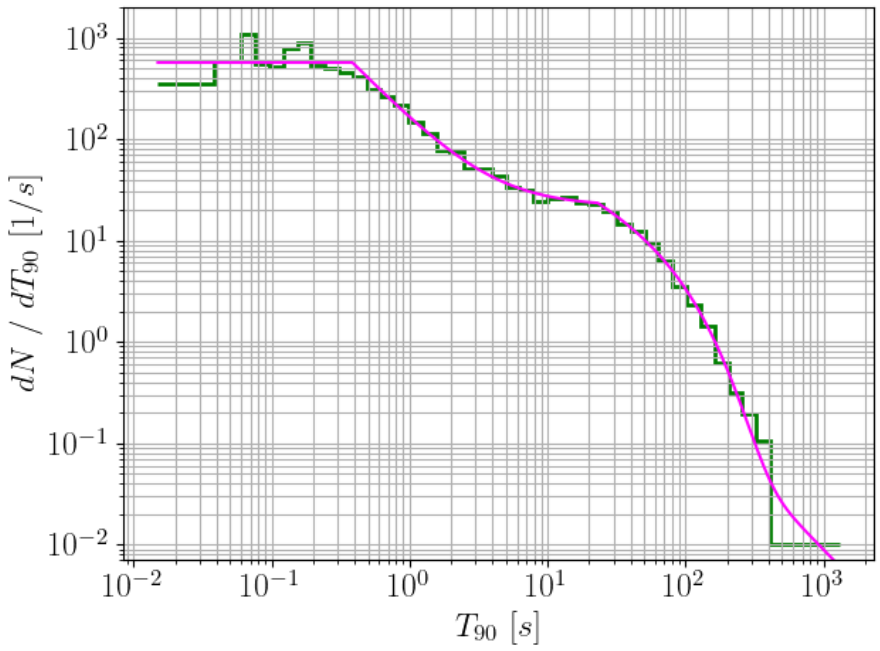

Figure 4.3: Comparing the fit of the best plateau plus powerlaw & plateau plus tapered powerlaw mixture model (pink) to the BATSE dataset (green) of T_{90} values. The BIC for this model is 8354.

The first model considered was a lognormal & lognormal mixture model. It posits that the underlying T_{90} distribution is a mixture of a lognormal model for short durations, and another lognormal model for long durations, as seen in Figure 4.2. Our hypothesis was that this is the most likely model, as there is no intrinsic plateau. It is a model of 5 parameters, and yields a BIC of 8339.

The second model considered was a plateau plus powerlaw & plateau plus powerlaw (tapered) mixture model. It posits that the underlying T_{90} distribution is a mixture of a plateau plus a powerlaw model for short durations, and a plateau plus a powerlaw model that is tapered for long durations, as seen in Figure 4.3. This is the model hypothesized by Moharana and Piran (2017) as most likely, as it has plateaus in both the short duration and long duration portions of the distribution. It is a model of 6 parameters, and yields a BIC of 8354.

The third model considered was a lognormal & plateau plus powerlaw (ta-

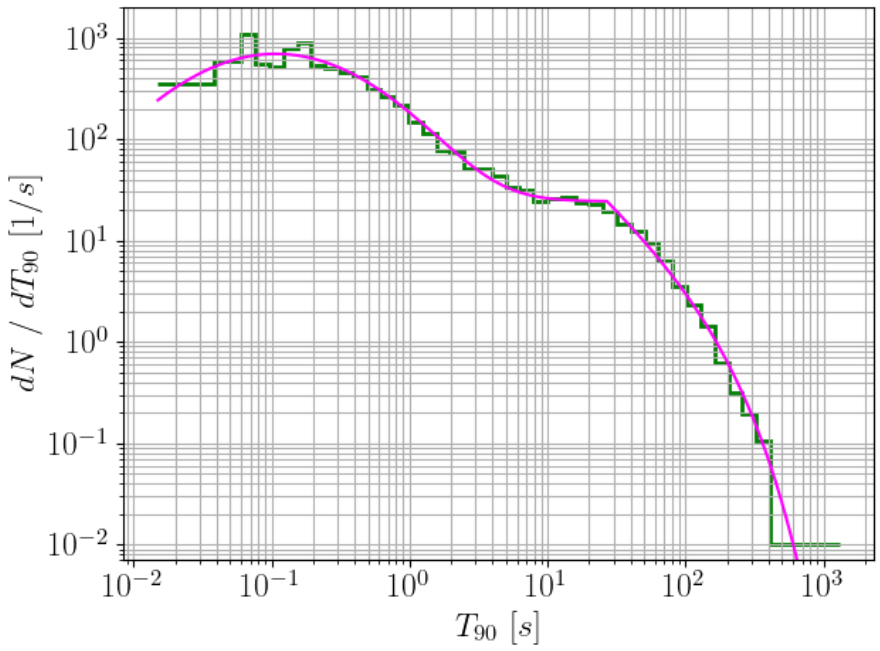

Figure 4.4: Comparing the fit of the best lognormal & plateau plus tapered powerlaw mixture model (pink) to the BATSE dataset (green) of T_{90} values. The BIC for this model is 8360.

pered) mixture model. It posits that the underlying T_{90} distribution is a mixture of a lognormal model for short durations, and a plateau plus a powerlaw model that is tapered for long durations, as seen in Figure 4.4. This is similar to the model proposed by Bromberg, Nakar, Piran, et al. (2012, 2013), that included a plateau in the long duration. It is a model of 6 parameters, and yields a BIC of 8360.

The final model considered was a plateau plus powerlaw & lognormal mixture model. It posits that the underlying T_{90} distribution is a mixture of a plateau plus a powerlaw model for short durations, and a lognormal model for long durations, as seen in Figure 4.5. It is a model of 5 parameters, and yields a BIC of 8362.

Of these four models, the lognormal & lognormal mixture model has the lowest BIC value, confirming our hypothesis that it is the most likely. Its BF indicates that it is on the order of ~10^3 times more likely than the double plateau model pro-

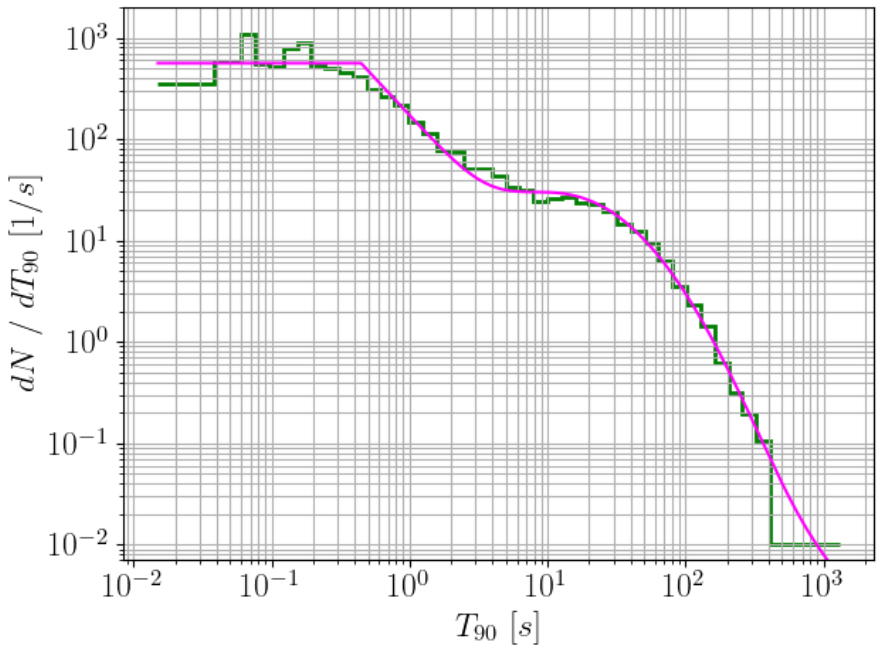

Figure 4.5: Comparing the fit of the best plateau plus powerlaw & log-normal mixture model (pink) to the BATSE dataset (green) of T_{90} values. The BIC for this model is 8362, the highest (i.e., worst fit) of the four models.

posed by Moharana and Piran (2017), and on the order of ~10^4 times[1] more likely than the single plateau model proposed by Bromberg, Nakar, Piran, et al. (2012, 2013). The BIC strongly suggests that plateaus are not intrinsic to the BATSE T_{90} dataset, or in the very least, that the plateau plus powerlaw models examined are not sufficiently representative of the data.

4.3 Concluding Remarks

The significance of these studies extend beyond the realm of GRB datasets. By improving statistical practices in astrophysics, this research has the potential to influence other fields that rely on complex data analysis.

Drawing conclusions from limited data is fundamental to the scientific process

[1] A correction must be noted here, as these values were originally reported incorrectly in Section 3.4. They have been corrected here.

and is an inherent aspect of research. We often work with incomplete or imperfect data due to various constraints, such as limited resources, observational capabilities, or the sheer complexity of natural phenomena. Without careful attention to the ways in which data might be potentially incomplete, inferences drawn about it can be misleading. This is particularly problematic if the missing data is not missing at random (e.g., missing systematically due to bias). This challenge necessitates the use of sophisticated statistical methods and analytical techniques to develop rigorous models and identify patterns or trends, without overfitting to random fluctuations and noise. We must carefully consider the limitations of our data, explicitly acknowledging any potential biases or uncertainties in our analyses in order to avoid drawing erroneous inferences. Fortunately, the iterative nature of science means that initial findings based on limited data often serve as a foundation for further investigation. As more data becomes available, hypotheses can be refined, models can be improved, and conclusions can be validated or revised. This continual process of testing, refinement, and validation is what drives scientific progress.

Bibliography

Abbott, Benjamin P et al. (2017a). "GW170817: observation of gravitational waves from a binary neutron star inspiral". In: *Physical Review Letters* 119.16, p. 161101.

Abbott, BP et al. (2017b). "Multi-messenger observations of a binary neutron star merger". In: *THE ASTROPHYSICAL JOURNAL LETTERS* 848.2, p. L12.

Atteia, J-L et al. (2017). "The maximum isotropic energy of gamma-ray bursts". In: *The Astrophysical Journal* 837.2, p. 119.

Balazs, Lajos G et al. (2003). "On the difference between the short and long gamma-ray bursts". In: *Astronomy & Astrophysics* 401.1, pp. 129–140.

Band, D et al. (1993). "BATSE observations of gamma-ray burst spectra. I-Spectral diversity". In: *The Astrophysical Journal* 413, pp. 281–292.

Band, David L and Robert D Preece (2005). "Testing the gamma-ray burst energy relationships". In: *The Astrophysical Journal* 627.1, p. 319.

Berger, Edo (2014). "Short-duration gamma-ray bursts". In: *Annual review of Astronomy and Astrophysics* 52, pp. 43–105.

Berger, Edo, W Fong, and R Chornock (2013). "An r-process kilonova associated with the short-hard GRB 130603B". In: *The Astrophysical Journal Letters* 774.2, p. L23.

Berkhuijsen, Elly M and Andrew Fletcher (2012). "Density PDFs of diffuse gas in the Milky Way". In: *European Astronomical Society Publications Series* 56, pp. 243–246.

Bloom, Joshua S, Dale A Frail, and Re'em Sari (2001). "The prompt energy release of gamma-ray bursts using a cosmological k-correction". In: *The Astronomical Journal* 121.6, p. 2879.

Bloom, Joshua S et al. (2002). "Detection of a supernova signature associated with GRB 011121". In: *the Astrophysical Journal Letters* 572.1, p. L45.

Bromberg, Omer, Ehud Nakar, and Tsvi Piran (2011). "Are low-luminosity gamma-ray bursts generated by relativistic jets?" In: *The Astrophysical Journal Letters* 739.2, p. L55.

Bromberg, Omer, Ehud Nakar, Tsvi Piran, et al. (2012). "An observational imprint of the collapsar model of long gamma-ray bursts". In: *The Astrophysical Journal* 749.2, p. 110.

– (2013). "Short versus long and collapsars versus non-collapsars: a quantitative classification of gamma-ray bursts". In: *The Astrophysical Journal* 764.2, p. 179.

Bryant, Christopher Michael, Joshua Alexander Osborne, and Amir Shahmoradi (2021). "How unbiased statistical methods lead to biased scientific discoveries: A case study of the Efron–Petrosian statistic applied to the luminosity-redshift evolution of gamma-ray bursts". In: *Monthly Notices of the Royal Astronomical Society* 504.3, pp. 4192–4203.

Butler, Nathaniel R, Joshua S Bloom, and Dovi Poznanski (2010). "The cosmic rate, luminosity function, and intrinsic correlations of long gamma-ray bursts". In: *The Astrophysical Journal* 711.1, p. 495.

Butler, Nathaniel R, Daniel Kocevski, and Joshua S Bloom (2009). "Generalized tests for selection effects in gamma-ray burst high-energy correlations". In: *The Astrophysical Journal* 694.1, p. 76.

Butler, Nathaniel R et al. (2007). "A complete catalog of Swift gamma-ray burst spectra and durations: demise of a physical origin for pre-Swift high-energy correlations". In: *The Astrophysical Journal* 671.1, p. 656.

Christensen, Lise, J Hjorth, and J Gorosabel (2004). "UV star-formation rates of GRB host galaxies". In: *Astronomy & Astrophysics* 425.3, pp. 913–926.

Collaboration, Fermi-LAT et al. (2018). "A gamma-ray determination of the Universe's star formation history". In: *Science* 362.6418, pp. 1031–1034.

Coward, DM et al. (2013). "The Swift gamma-ray burst redshift distribution: selection biases and optical brightness evolution at high z?" In: *Monthly Notices of the Royal Astronomical Society* 432.3, pp. 2141–2149.

Coward, DM et al. (2015). "Selection biases in the gamma-ray burst E iso–L opt, X correlation". In: *Monthly Notices of the Royal Astronomical Society: Letters* 449.1, pp. L6–L10.

Cucchiara, A et al. (2011). "A Photometric Redshift of z 9.4 for GRB 090429B". In: *The Astrophysical Journal* 736.1, p. 7.

Dainotti, Maria Giovanna, Jack Singal, Michal Ostrowski, et al. (2013). "Determination of the intrinsic luminosity time correlation in the X-ray afterglows of gamma-ray bursts". In: *The Astrophysical Journal* 774.2, p. 157.

D'Avanzo, P (2015). "Short gamma-ray bursts: A review". In: *Journal of High Energy Astrophysics* 7, pp. 73–80.

Deng, Can-Min et al. (2016). "Cosmic Evolution of Long Gamma-Ray Burst Luminosity". In: *The Astrophysical Journal* 820.1, p. 66.

Duffell, Paul C, Eliot Quataert, and Andrew I MacFadyen (2015). "A narrow short-duration GRB jet from a wide central engine". In: *The Astrophysical Journal* 813.1, p. 64.

Efron, Bradley and Vahé Petrosian (1992). "A simple test of independence for truncated data with applications to redshift surveys". In: *The Astrophysical Journal* 399, pp. 345–352.

Eichler, David et al. (1989). "Nucleosynthesis, neutrino bursts and γ-rays from coalescing neutron stars". In: *Nature* 340.6229, pp. 126–128.

Fenimore, EE et al. (2003). "The Trigger Algorithm for the Burst Alert Telescope on Swift". In: *AIP Conference Proceedings*. Vol. 662. 1. American Institute of Physics, pp. 491–493.

Fishman, Gerald J et al. (1994). "The first BATSE gamma-ray burst catalog". In: *The Astrophysical Journal Supplement Series* 92, pp. 229–283.

Fong, Wen-fai et al. (2012). "A jet break in the X-ray light curve of short GRB 111020A: implications for energetics and rates". In: *The Astrophysical Journal* 756.2, p. 189.

Fruchter, AS et al. (2006). "Long γ-ray bursts and core-collapse supernovae have different environments". In: *Nature* 441.7092, pp. 463–468.

Galama, Titus J et al. (1998). "An unusual supernova in the error box of the γ-ray burst of 25 April 1998". In: *nature* 395.6703, pp. 670–672.

Gehrels, N, E Chipman, and DA Kniffen (1993). "The Compton Gamma Ray Observatory". In: *Astronomy and Astrophysics Supplement Series (ISSN 0365-0138), vol. 97, no. 1, p. 5-12.* 97, pp. 5–12.

Gehrels, Neil, E Ramirez-Ruiz, and Derek B Fox (2009). "Gamma-ray bursts in the Swift era". In: *Annual Review of Astronomy and Astrophysics* 47, pp. 567–617.

Ghirlanda, Giancarlo et al. (2015). "Are short Gamma Ray Bursts similar to long ones?" In: *Journal of High Energy Astrophysics* 7, pp. 81–89.

Ghirlanda, Giancarlo et al. (2019). "Compact radio emission indicates a structured jet was produced by a binary neutron star merger". In: *Science* 363.6430, pp. 968–971.

Glendenning, Norman K (2012). *Compact stars: Nuclear physics, particle physics and general relativity*. Springer Science & Business Media.

Goldstein, A et al. (2017). "An ordinary short gamma-ray burst with extraordinary implications: Fermi-GBM detection of GRB 170817A". In: *The Astrophysical Journal Letters* 848.2, p. L14.

Goldstein, Adam et al. (2013). "The BATSE 5B gamma-ray burst spectral catalog". In: *The Astrophysical Journal Supplement Series* 208.2, p. 21.

Gottlieb, Ore, Ehud Nakar, and Tsvi Piran (2018). "The cocoon emission–an electromagnetic counterpart to gravitational waves from neutron star mergers". In: *Monthly Notices of the Royal Astronomical Society* 473.1, pp. 576–584.

Hakkila, Jon et al. (2003). "How sample completeness affects gamma-ray burst classification". In: *The Astrophysical Journal* 582.1, p. 320.

Harrison, FA et al. (1999). "Optical and Radio Observations of the Afterglow from GRB 990510: Evidence for a Jet". In: *The Astrophysical Journal* 523.2, p. L121.

Hjorth, J et al. (2011). "Gamma-Ray Bursts". In: *Cambridge Astrophysics Series, ed. C. Kouveliotou, RAMJ Wijers, & S. Woosley (Cambridge: Cambridge Univ. Press)* 51.

Hjorth, Jens et al. (2003). "A very energetic supernova associated with the γ-ray burst of 29 March 2003". In: *Nature* 423.6942, pp. 847–850.

Hopkins, Andrew M and John F Beacom (2006). "On the normalization of the cosmic star formation history". In: *The Astrophysical Journal* 651.1, p. 142.

Klebesadel, Ray W, Ian B Strong, and Roy A Olson (1973). "Observations of gamma-ray bursts of cosmic origin". In: *The Astrophysical Journal* 182, p. L85.

Kocevski, Dan and Edison Liang (2006). "Quantifying the luminosity evolution in gamma-ray bursts". In: *The Astrophysical Journal* 642.1, p. 371.

Koshut, Thomas M et al. (1995). "Gamma-ray burst precursor activity as observed with BATSE". In: *Astrophysical Journal v. 452, p. 145* 452, p. 145.

Kouveliotou, Chryssa et al. (1993). "Identification of two classes of gamma-ray bursts". In: *The Astrophysical Journal* 413, pp. L101–L104.

Krühler, T et al. (2015). "GRB hosts through cosmic time-VLT/X-Shooter emission-line spectroscopy of 96 γ-ray-burst-selected galaxies at $0.1< z< 3.6$". In: *Astronomy & Astrophysics* 581, A125.

Kumar, Pawan and Bing Zhang (2015). "The physics of gamma-ray bursts & relativistic jets". In: *Physics Reports* 561, pp. 1–109.

Kumbhare, Shashank and Amir Shahmoradi (Sept. 2020). "MatDRAM: A pure-MATLAB Delayed-Rejection Adaptive Metropolis-Hastings Markov Chain Monte Carlo Sampler". In: *arXiv e-prints*, arXiv:2010.04190, arXiv:2010.04190. arXiv: 2010.04190 [cs.MS].

Lan, Guang-Xuan et al. (2019). "The luminosity function and formation rate of a complete sample of long gamma-ray bursts". In: *Monthly Notices of the Royal Astronomical Society* 488.4, pp. 4607–4613.

Le, Truong, Cecilia Ratke, and Vedant Mehta (2020). "Resolving the excess of long GRB's at low redshift in the Swift era". In: *Monthly Notices of the Royal Astronomical Society* 493.1, pp. 1479–1491.

Le Floc'h, Emeric et al. (2003). "Are the hosts of gamma-ray bursts sub-luminous and blue galaxies?" In: *Astronomy & Astrophysics* 400.2, pp. 499–510.

Levan, Andrew et al. (2023). "JWST detection of heavy neutron capture elements in a compact object merger". In: *arXiv preprint arXiv:2307.02098*.

Lloyd, Nicole M and Vahé Petrosian (1999). "Distribution of spectral characteristics and the cosmological evolution of gamma-ray bursts". In: *The Astrophysical Journal* 511.2, p. 550.

Lloyd, Nicole M, Vahé Petrosian, and Robert S Mallozzi (2000). "Cosmological versus Intrinsic: The Correlation between Intensity and the Peak of the $\nu F\nu$ Spectrum of Gamma-Ray Bursts". In: *The Astrophysical Journal* 534.1, p. 227.

Lloyd-Ronning, Nicole M, Aycin Aykutalp, and Jarrett L Johnson (2019). "On the cosmological evolution of long gamma-ray burst properties". In: *Monthly Notices of the Royal Astronomical Society* 488.4, pp. 5823–5832.

London III, John R (1993). "VELA-A space system success story". In: *Acta Astronautica* 29.9, pp. 723–734.

Lynden-Bell, D (1971). "A method of allowing for known observational selection in small samples applied to 3CR quasars". In: *Monthly Notices of the Royal Astronomical Society* 155.1, pp. 95–118.

MacFadyen, AI and SE Woosley (1999). "Collapsars: Gamma-ray bursts and explosions in "failed supernovae"". In: *The Astrophysical Journal* 524.1, p. 262.

MacFadyen, Andrew I, SE Woosley, and A Heger (2001). "Supernovae, jets, and collapsars". In: *The Astrophysical Journal* 550.1, p. 410.

Madau, Piero and Tassos Fragos (2017). "Radiation backgrounds at cosmic dawn: X-rays from compact binaries". In: *The Astrophysical Journal* 840.1, p. 39.

Massey, Philip (1981). "The masses of Wolf-Rayet stars". In: *Astrophysical Journal, Part 1, vol. 246, May 15, 1981, p. 153-160.* 246, pp. 153–160.

Medvedev, AS et al. (2017). "Statistics of magnetic field measurements in OBA stars and the evolution of their magnetic fields". In: *Astronomische Nachrichten* 338.8, pp. 910–918.

Mészáros, P and MJ Rees (1997). "Optical and long-wavelength afterglow from gamma-ray bursts". In: *The Astrophysical Journal* 476.1, p. 232.

Metzger, Brian D and Edo Berger (2012). "What is the most promising electromagnetic counterpart of a neutron star binary merger?" In: *The Astrophysical Journal* 746.1, p. 48.

Metzger, Brian D et al. (2010). "Electromagnetic counterparts of compact object mergers powered by the radioactive decay of r-process nuclei". In: *Monthly Notices of the Royal Astronomical Society* 406.4, pp. 2650–2662.

Moharana, Reetanjali and Tsvi Piran (2017). "Observational evidence for mass ejection accompanying short gamma-ray bursts". In: *Monthly Notices of the Royal Astronomical Society: Letters* 472.1, pp. L55–L59.

Mooley, KP et al. (2018). "Superluminal motion of a relativistic jet in the neutron-star merger GW170817". In: *Nature* 561.7723, pp. 355–359.

Murguia-Berthier, Ariadna et al. (2014). "Necessary conditions for short gamma-ray burst production in binary neutron star mergers". In: *The Astrophysical Journal Letters* 788.1, p. L8.

Mészáros, Peter (2006). "Gamma-ray bursts". In: *Reports on Progress in Physics* 69.8, p. 2259.

Nagakura, Hiroki et al. (2014). "Jet collimation in the ejecta of double neutron star mergers: a new canonical picture of short gamma-ray bursts". In: *The Astrophysical Journal Letters* 784.2, p. L28.

Nakar, Ehud (2007). "Short-hard gamma-ray bursts". In: *Physics Reports* 442.1-6, pp. 166–236.

Nakar, Ehud and Tsvi Piran (2004). "Outliers to the isotropic energy-Peak energy relation in GRBs". In: *Mon. Not. Roy. Astron. Soc.* 360.astro-ph/0412232, p. 73.

Narayan, Ramesh, Tsvi Piran, and Pawan Kumar (2001). "Accretion models of gamma-ray bursts". In: *The Astrophysical Journal* 557.2, p. 949.

Osborne, Joshua A, Fatemeh Bagheri, and Amir Shahmoradi (2021). "Are there radio-loud and radio-quiet gamma-ray bursts?" In: *Monthly Notices of the Royal Astronomical Society* 502.4, pp. 5622–5630.

Osborne, Joshua A, Amir Shahmoradi, and Robert J Nemiroff (2020). "A multi-level empirical bayesian approach to estimating the unknown redshifts of 1366 batse catalog long-duration gamma-ray bursts". In: *The Astrophysical Journal* 903.1, p. 33.

Osborne, Joshua Alexander et al. (2023). "An alternative statistical interpretation for the first direct evidence of Collapsars". In: *arXiv e-prints*, arXiv–2310.

Paciesas, William S et al. (1999). "The fourth BATSE gamma-ray burst catalog (revised)". In: *The Astrophysical Journal Supplement Series* 122.2, p. 465.

Panaitescu, A and P Mészáros (1999). “Dynamical evolution, light curves, and spectra of spherical and collimated gamma-ray burst remnants”. In: *The Astrophysical Journal* 526.2, p. 707.

Perley, DA et al. (2015). “Connecting GRBs and ULIRGs: a sensitive, unbiased survey for radio emission from gamma-ray burst host galaxies at 0< z< 2.5”. In: *The Astrophysical Journal* 801.2, p. 102.

Perley, DA et al. (2016a). “The swift GRB host galaxy legacy survey. ii. rest-frame near-ir luminosity distribution and evidence for a near-solar metallicity threshold”. In: *The Astrophysical Journal* 817.1, p. 8.

Perley, Daniel A et al. (2016b). “The Swift gamma-ray burst host galaxy legacy survey. I. Sample selection and redshift distribution”. In: *The Astrophysical Journal* 817.1, p. 7.

Pescalli, A et al. (2016). “The rate and luminosity function of long gamma ray bursts”. In: *Astronomy & Astrophysics* 587, A40.

Petrosian, Vahe (2002). “New statistical methods for analysis of large surveys: distributions and correlations”. In: *International Astronomical Union Colloquium*. Vol. 184. Cambridge University Press, pp. 389–397.

Petrosian, Vahé, Ellie Kitanidis, and Daniel Kocevski (2015). “Cosmological evolution of long gamma-ray bursts and the star formation rate”. In: *ApJ* 806.1, p. 44.

Petrosian, Vahé and Theodore T Lee (1996). “The Fluence distribution of gamma-ray bursts”. In: *The Astrophysical Journal Letters* 467.1, p. L29.

Petrosian, Vahe’, Nicole M Lloyd-Ronning, and Andrew Lee (1999). “Cosmological signatures in temporal and spectral characteristics of gamma-ray bursts”. In: *arXiv preprint astro-ph/9906393*.

Pe’Er, Asaf (2015). “Physics of Gamma-Ray Bursts Prompt Emission”. In: *Advances in Astronomy* 2015.1, p. 907321.

Poolakkil, S et al. (2021). "The Fermi-GBM Gamma-Ray Burst spectral catalog: 10 yr of data". In: *The Astrophysical Journal* 913.1, p. 60.

Rhoads, James E (1997). "How to tell a jet from a balloon: a proposed test for beaming in gamma-ray bursts". In: *The Astrophysical Journal* 487.1, p. L1.

– (1999). "The dynamics and light curves of beamed gamma-ray burst afterglows". In: *The Astrophysical Journal* 525.2, p. 737.

Salafia, OS et al. (2020). "Gamma-ray burst jet propagation, development of angular structure, and the luminosity function". In: *Astronomy & Astrophysics* 636, A105.

Salvaterra, R et al. (2012). "A complete sample of bright Swift long gamma-ray bursts. I. Sample presentation, luminosity function and evolution". In: *The Astrophysical Journal* 749.1, p. 68.

Savchenko, Volodymyr et al. (2017a). "INTEGRAL detection of the first prompt gamma-ray signal coincident with the gravitational-wave event GW170817". In: *The Astrophysical Journal Letters* 848.2, p. L15.

Savchenko, Volodymyr et al. (2017b). "INTEGRAL follow-up of the gravitational wave events". In: *PoS, vol. IFS2017*, p. 058.

Schulze, Steve et al. (2015). "The Optically Unbiased GRB Host (TOUGH) Survey. VII. The Host Galaxy Luminosity Function: Probing the Relationship between GRBs and Star Formation to Redshift 6". In: *The Astrophysical Journal* 808.1, p. 73.

Schwarz, Gideon et al. (1978). "Estimating the dimension of a model". In: *The annals of statistics* 6.2, pp. 461–464.

Shahmoradi, Amir (2013a). "A Multivariate Fit Luminosity Function and World Model for Long Gamma-Ray Bursts". In: *ApJ* 766.2, p. 111.

– (2013b). "Gamma-Ray bursts: Energetics and Prompt Correlations". In: *arXiv e-prints*, arXiv:1308.1097, arXiv:1308.1097. arXiv: 1308.1097 [astro-ph.HE].

– (2017). “Multilevel Bayesian Parameter Estimation in the Presence of Model Inadequacy and Data Uncertainty”. In: *arXiv preprint arXiv:1711.10599*.

Shahmoradi, Amir (Nov. 2017). “Multilevel Bayesian Parameter Estimation in the Presence of Model Inadequacy and Data Uncertainty”. In: *arXiv e-prints*, arXiv:1711.10599, arXiv:1711.10599. arXiv: 1711.10599 [physics.data-an].

Shahmoradi, Amir (2019). “ParaMonte: A user-friendly parallel Monte Carlo optimization, sampling, and integration library for scientific inference”. In: *APS March Meeting Abstracts*. Vol. 2019, G70–292.

Shahmoradi, Amir and Fatemeh Bagheri (Aug. 2020). “ParaDRAM: A Cross-Language Toolbox for Parallel High-Performance Delayed-Rejection Adaptive Metropolis Markov Chain Monte Carlo Simulations”. In: *arXiv e-prints*, arXiv:2008.09589, arXiv:2008.09589. arXiv: 2008.09589 [cs.CE].

Shahmoradi, Amir and Fatemeh Bagheri (Aug. 2020a). “ParaDRAM: A Cross-Language Toolbox for Parallel High-Performance Delayed-Rejection Adaptive Metropolis Markov Chain Monte Carlo Simulations”. In: *Computer Methods in Applied Mechanics and Engineering (under review)*, arXiv:2008.09589, arXiv:2008.09589. arXiv: 2008.09589 [cs.CE].

– (2020b). “ParaDRAM: A Cross-Language Toolbox for Parallel High-Performance Delayed-Rejection Adaptive Metropolis Markov Chain Monte Carlo Simulations”. In: *arXiv preprint arXiv:2008.09589*.

– (2020c). *ParaMonte: A high-performance serial/parallel Monte Carlo simulation library for C, C++, Fortran*. arXiv: 2009.14229 [cs.MS]. URL: https://arxiv.org/abs/2009.14229.

Shahmoradi, Amir and Fatemeh Bagheri (May 2021). “ParaMonte: A high-performance serial/parallel Monte Carlo simulation library for C, C++, Fortran”. In: *The Journal of Open Source Software* 6.61, p. 2741. DOI: 10.21105/joss.02741. arXiv: 2009.14229 [cs.MS].

Shahmoradi, Amir, Fatemeh Bagheri, and Joshua Alexand er Osborne (Oct. 2020). "Fast fully-reproducible serial/parallel Monte Carlo and MCMC simulations and visualizations via ParaMonte::Python library". In: *arXiv e-prints*, arXiv:2010.00724, arXiv:2010.00724. arXiv: 2010.00724 [cs.MS].

Shahmoradi, Amir and RJ Nemiroff (2011a). "A Cosmological Discriminator Designed to Avoid Selection Bias". In: *Bulletin of the American Astronomical Society*. Vol. 43.

Shahmoradi, Amir and Robert Nemiroff (2009). "How Real detector thresholds create false standard candles". In: *AIP Conference Proceedings*. Vol. 1133. 1. AIP, pp. 425–427.

Shahmoradi, Amir and Robert J Nemiroff (2010). "Hardness as a spectral peak estimator for gamma-ray bursts". In: *Monthly Notices of the Royal Astronomical Society* 407.4, pp. 2075–2090.

Shahmoradi, Amir and Robert J Nemiroff (2011b). "The possible impact of gamma-ray burst detector thresholds on cosmological standard candles". In: *MNRAS* 411.3, pp. 1843–1856.

– (2015). "Short versus long gamma-ray bursts: a comprehensive study of energetics and prompt gamma-ray correlations". In: *MNRAS* 451.1, pp. 126–143.

Shahmoradi, Amir and Robert J. Nemiroff (Mar. 2019). "A Catalog of Redshift Estimates for 1366 BATSE Long-Duration Gamma-Ray Bursts: Evidence for Strong Selection Effects on the Phenomenological Prompt Gamma-Ray Correlations". In: *arXiv e-prints*, arXiv:1903.06989, arXiv:1903.06989. arXiv: 1903.06989 [astro-ph.HE].

Singal, Jack, V Petrosian, A Lawrence, et al. (2011). "On the Radio and Optical Luminosity Evolution of Quasars". In: *The Astrophysical Journal* 743.2, p. 104.

Soderberg, Alicia M et al. (2006). "Relativistic ejecta from X-ray flash XRF 060218 and the rate of cosmic explosions". In: *Nature* 442.7106, pp. 1014–1017.

Stanek, Krzysztof Z et al. (2003). "Spectroscopic discovery of the supernova 2003dh associated with GRB 030329". In: *The Astrophysical Journal* 591.1, p. L17.

Strong, Ian B, Ray W Klebesadel, and Roy A Olson (1974). "A preliminary catalog of transient cosmic gamma-ray sources observed by the VELA satellites". In: *Astrophysical Journal, vol. 188, p. L1* 188, p. L1.

Tanvir, NR et al. (2013). "A 'kilonova' associated with the short-duration γ-ray burst GRB 130603B". In: *Nature* 500.7464, pp. 547–549.

Tarnopolski, Mariusz (2021). "How does the shape of gamma-ray bursts' pulses affect the duration distribution?" In: *Monthly Notices of the Royal Astronomical Society* 507.1, pp. 1450–1457.

Taylor, GB et al. (2004). "The angular size and proper motion of the afterglow of GRB 030329". In: *The Astrophysical Journal* 609.1, p. L1.

Troja, E et al. (2022). "A nearby long gamma-ray burst from a merger of compact objects". In: *Nature* 612.7939, pp. 228–231.

Tsvetkova, A et al. (2017). "The Konus-Wind catalog of gamma-ray bursts with known redshifts. I. Bursts detected in the triggered mode". In: *arXiv preprint arXiv:1710.08746*.

Usov, VV (1992). "Millisecond pulsars with extremely strong magnetic fields as a cosmological source of γ-ray bursts". In: *Nature* 357.6378, pp. 472–474.

Vergani, SD et al. (2015). "Are long gamma-ray bursts biased tracers of star formation? Clues from the host galaxies of the Swift/BAT6 complete sample of LGRBs-I. Stellar mass at z< 1". In: *Astronomy & Astrophysics* 581, A102.

Wagenmakers, Eric-Jan (2007). "A practical solution to the pervasive problems of p values". In: *Psychonomic bulletin & review* 14.5, pp. 779–804.

Wang, Feifei et al. (2020). "A Comprehensive Statistical Study of Gamma-Ray Bursts". In: *The Astrophysical Journal* 893.1, p. 77.

Wickramasinghe, T and TN Ukwatta (2010). "An analytical approach for the determination of the luminosity distance in a flat universe with dark energy". In: *Monthly Notices of the Royal Astronomical Society* 406.1, pp. 548–550.

Woosley, SE and JS Bloom (2006). "The supernova–gamma-ray burst connection". In: *Annu. Rev. Astron. Astrophys.* 44, pp. 507–556.

Woosley, SE and Alexander Heger (2006). "The progenitor stars of gamma-ray bursts". In: *The Astrophysical Journal* 637.2, p. 914.

Woosley, Stan E (1993). "Gamma-ray bursts from stellar mass accretion disks around black holes". In: *The Astrophysical Journal* 405, pp. 273–277.

Yan, Y et al. (2021). "Characteristic time of stellar flares on Sun-like stars". In: *Monthly Notices of the Royal Astronomical Society: Letters* 505.1, pp. L79–L83.

Yang, Bin et al. (2015). "A possible macronova in the late afterglow of the long–short burst GRB 060614". In: *Nature Communications* 6.1, pp. 1–5.

Yu, H et al. (2015). "An unexpectedly low-redshift excess of Swift gamma-ray burst rate". In: *The Astrophysical Journal Supplement Series* 218.1, p. 13.

Zaninetti, Lorenzo (2018). "A lognormal luminosity function for SWIRE in flat cosmology". In: *arXiv preprint arXiv:1811.01579*.

Zhang, Bing (2007). "Gamma-ray bursts in the Swift era". In: *Chinese Journal of Astronomy and Astrophysics* 7.1, p. 1.

Zhang, Bing and Peter Mészáros (2001). "Gamma-ray burst afterglow with continuous energy injection: signature of a highly magnetized millisecond pulsar". In: *The Astrophysical Journal* 552.1, p. L35.